The Impacts of Dust on Regional Tropospheric Chemistry During the ACE-ASIA Experiment: A Model Study with Observations

Youhua Tang[1], Gregory R. Carmichael[1], Gakuji Kurata[2], Itsushi Uno[3], Rodney J. Weber[4], Chul-Han Song[4], Sarath K. Guttikunda[1], Jung-Hun Woo[1], David G. Streets[5], Cao Wei[1], Antony D. Clarke[6], Barry Huebert[6], and Theodore L. Anderson[7]

1 Center for Global and Regional Environmental Research, University of Iowa, Iowa, USA
2 Department of Ecological Engineering, Toyohashi University of Technology, Toyohashi, Japan
3 Research Institute for Applied Mechanics, Kyushu University, Fukuoka, Japan
4 School of Earth and Atmospheric Sciences, Georgia Institute of Technology, Georgia, USA
5 Decision and Information Sciences Division, Argonne National Laboratory, Illinois, USA
6 School of Ocean and Earth Science and Technology, University of Hawaii, Hawaii, USA
7 Department of Atmospheric Science, University of Washington, Seattle, WA, USA

Abstract:

A comprehensive regional-scale chemical transport model, STEM-2K1, is employed to study dust outflows and their influence on regional chemistry in the high dust ACE-ASIA period, from April 4 to 14, 2001. In this period, dust storms are initialized in the Taklamagan and Gobi deserts due to cold air outbreaks, are transported eastward, and often intensified by dust emitted from exposed soils as the front moves off the continent. Simulated dust agrees well with surface weather observations, satellite images, and the measurements of the C-130 aircraft. The C-130 aircraft observations of chemical constituents of the aerosol are analyzed for dust-rich and low dust periods. In the sub-micron aerosol, dust-rich air masses have elevated ratios of $\Delta Ca/\Delta Mg$, $\Delta NH_4^+ / \Delta SO_4^{2-}$, $\Delta NO_3^-/\Delta CO$ (Δ represents the difference between observed and background concentrations). The impacts of heterogeneous reactions on dust involving O_3, NO_2, SO_2 and HNO_3 are studied by incorporating these reactions into the analysis. These reactions have significant influence on regional chemistry. For example, the low O_3 concentrations in the C-130 flight 6 can be explained only by the influence of heterogeneous reactions. In the near-surface layer, the modeled heterogeneous reactions indicated that O_3, SO_2, NO_2 and HNO_3 are decreased by up to 20%, 55%, 20% and 95%, respectively when averaged over this period. In addition, NO, HONO and daytime OH can increase by 20%, 30%, and 4%, respectively, over polluted regions. When dust

encounters fresh pollutants, these heterogeneous reactions can lead to a series of complex responses of the photochemical system. In addition, these reactions can alter the chemical-size distribution of the aerosol. Under heavy dust loadings, these reactions can lead to > 20% of the sulfate and >70% of the nitrate being associated with the coarse fraction. The radiative influence of dust can also affect the photochemical system. For example, OH levels can decrease by 20% near surface. The dust radiative influence is shown to be weaker than the heterogeneous influence for most species.

1. Introduction

The Aerosol Characterization Experiment in Asia (ACE-ASIA) field campaign was performed in East Asia from late March to early May, 2001. This experiment, together with the TRACE-P (TRAnsport & Chemical Evolution over the Pacific) experiment conducted from mid-February to mid-April, 2001, produced detailed observational data sets on aerosols and trace gases in this region. In this season, strong dust storms occurred and were sampled by both TRACE-P (Jordan et al., 2003) and ACE-ASIA (Huebert et al., this issue) experiments. The TRACE-P measurements mainly focused on gas-phase species and other associated physical variables. In ACE-ASIA, measurements were focused on aerosol properties and radiation.

Data from these experiments provide valuable insights into the impact of aerosols on atmospheric chemistry. Aerosols can impact atmospheric chemistry in several ways. They can affect the actinic flux and thus alter photolysis rates (Tang et al., 2003a). They can also provide surfaces upon which chemical reactions can occur (Dentener et al., 1996). In addition, through radiative forcing effects, they can change the regional temperature and cloud fields, which in turn may perturb the photochemical processes (Tang et al., 2003a; Conant et al., this issue). These impacts of aerosols on tropospheric chemistry remain poorly characterized. Because of the high aerosol loadings in Asia during spring, Asia is an excellent location to

investigate these effects. The comprehensive measurements obtained by ACE-ASIA and TRACE-P provide an excellent dataset to investigate and quantify these interactions.

Tang et al (2003a) investigated the impacts of aerosols on the photochemical oxidant cycle in Asia during TRACE-P using a modeling system that explicitly considered aerosol and cloud radiative influences. They compared measured photochemical species (O_3, OH, PAN, etc.), and measured photolysis rates, with calculated values. They found that Asian aerosols (which contain large amounts of carbonaceous material, inorganic components such as sulfates, and mineral oxides) significantly impacted photolysis frequencies (J-values) and photochemical processes. When averaged over all TRACE-P DC-8 and P-3B flights, the aerosol influence via affecting J-values was found to reduce OH by ~ 40% below 1km, and by ~ 24% from 1km to 10km. Furthermore, aerosols were shown to have a stronger impact on longer-lived chemical species than that due to clouds, because anthropogenic aerosols tend to be co-emitted with precursors and have a longer contact time with the polluted air masses. In megacity (population > 10 million) plumes, aerosols were found to increase NO_x concentrations by 40% via reducing its photolytic loss. This analysis did not investigate the contributions of individual aerosols types such as dust, nor did it consider aerosol impacts associated with heterogeneous reactions.

In this paper, we focus on the impacts of mineral aerosol on regional chemistry during the dust storm periods of ACE-ASIA. We evaluate the effects of dust on photolysis rates, and chemical interactions via heterogeneous reactions involving SO_2, NO_2, HNO_3 and O_3 using a three-dimensional chemical transport model, STEM 2K1, (Tang et al, 2003a). The period of 4-14 April, which contained several large dusts events, is the focus of this study, and provides an excellent opportunity to look for the impacts of dust. Data from three C-130 flights that measured various stages of this dust/pollution outbreak are compared with model calculations, and used to evaluate the influence of dust on the photochemical oxidant cycle,

and on sulfate and nitrate production. The model is then used to assess the impacts of the dust over the entire East Asia region during this period.

2. Simulation description

2.1 The STEM-2K1 Model

The three-dimensional model, STEM 2K1, (Tang et al, 2003a) was employed for this study. This model is a comprehensive regional-scale chemical transport model, with a detailed photochemical mechanism SAPRC 99 (Carter, 2000) and an explicit photolysis solver TUV (NCAR Tropospheric Ultraviolet-Visible radiation model) (Madronich and Flocke, 1999). This model system was also used in the analysis of the TRACE-P observations (Carmichael et al., 2003), and was shown to accurately represent many of the important observed features. A schematic of the processes treated in the analysis of the aerosol impacts are shown in Figure 1. To study the aerosol impacts on photolysis rates, TUV was implemented on-line with the transport and chemical processes. Thirty different photolysis rates were calculated. Photolysis rates were calculated column-wise, considering the influences of clouds, aerosols and gas-phase absorptions due to O_3, SO_2 and NO_2, for each horizontal grid point (on an 80 km grid spacing). The effects of clouds on photolysis rates were included, and cloud fields were calculated by the RAMS mesoscale meteorological model (as were all the meteorological fields used in this analysis). The optical properties of water clouds were calculated with a simple scheme (Madronich, 1987). Aerosols fields (black carbon (BC), organic carbon (OC), sulfate, sea salt, and wind blown dust) were calculated within the STEM-2K1 model. At each integrating time step, aerosol concentrations from the STEM main module were converted from mass concentrations to aerosol optical properties according to Hess et al. (1998). For this study the RAMS model was driven by ECMWF 1ºx1º reanalysis data. Since the TUV has a higher top (80km) than that of the chemical-transport domain (~15 km), ozone absorption in the model's overtop layers were accounted for by using the observed TOMS (Total Ozone Mapping Spectrometer)

total columns subtract modeled tropospheric ozone column. Further details regarding the STEM-2K1 and meteorological fields used in this analysis are available in Tang et al. (2003a) and Uno et al. (this issue).

In addition to the radiative influences, dust can be involved in heterogeneous reactions. Recent laboratory studies have measured a variety of chemical reactions involving metal oxide surfaces (Grassian, 2002). These studies indicate that dust surfaces can provide heterogeneous pathways for a variety of reactions including those involving SO_2, NO_2, HNO_3, and O_3. The mechanism and reaction rates vary by species and by surface. For example, reactions with nitric acid with calcium carbonate are not restricted to the surface, but rather can access the entire mass of the particle (Kruger et al., 2003). In contrast, reactions of NO_2 with dust at low relative humidity are limited to the surface, and slow down as products accumulate on the surface (Underwood et al., 2001). Reactions involving ozone appear to be catalytic and do not show such saturation effects (Michel et al., 2003). In this paper, we consider the following heterogeneous reactions on dust:

$$O_3 \xrightarrow{Dust} 1.5O_2$$
$$SO_2 \xrightarrow{Dust} Sulfate$$
$$NO_2 \xrightarrow{Dust} 0.5Nitrite + 0.5Nitrate$$
$$HNO_3 \xrightarrow{Dust} Nitrate$$

We treat these reactions in a simplified manner; i.e., the effects of relative humidity and saturation are not explicitly considered (Zhang and Carmichael, 1999). The uptake coefficients were assumed to be constant, with values for $\gamma(O_3)$, $\gamma(SO_2)$, $\gamma(NO_2)$ and $\gamma(HNO_3)$ of 5×10^{-5} (Michel et al., 2002, Dentener et al., 1996; Jacob 2000), 1×10^{-4} (Usher et al., 2002; Zhang and Carmichael, 1999; Phadnis and Carmichael, 2000; Goodman et al., 2001), 1×10^{-4} (Underwood et al. 2001) and 0.01 (Prince et al., 2002; Goodman et al., 2000; Hanisch and Crowley, 2001), respectively. In this paper, STEM-2K1 explicitly considers the transport of gas-phase and aerosol species, along with their chemical and radiative interactions.

2.2 Emission Estimates

The aerosol species considered in the analysis include dust, sea salt, black carbon (BC), organic carbon (OC), sulfate, other PM2.5 (non-carbonaceous, non wind-blown dust) and other PM10. Sea salt emissions were calculated on-line following Monahan et al (1986) and Song and Carmichael (2001). The energy-related primary aerosol and gaseous emissions used are as described in Streets et al. (2003), and the biomass burning emissions are presented in Woo et al. (2003). Tang et al. (2003a) described the detailed information about emissions used for TRACE-P and ACE-ASIA simulations.

Dust emissions were estimated using a modified form of the method of Liu and Westphal (2001). Total dust emissions were calculated using:

$$E_{dust} = A(U^* - U_{th})U^{*3} \quad \text{when } U^* > U_{th}$$

where E_{dust} is the dust emission flux in $g/m^2/s$, A is dimensional emission factor (equal to 4.5×10^{-4} in this study), U^* is surface friction speed in *m/s*, and U_{th} is the threshold U^*, values above which dusts can be emitted. In this study, a U_{th} value of 0.4 *m/s* is applied to Taklamagan desert and Loess plateau, and a value of 0.6 *m/s* is used for other arid and semi-arid regions. The emission factor A is determined by the upper limit of the dust particle diameter. Here we only consider the dust particles whose diameters are smaller than 10 μm, since these dust particles can be transported over sufficiently long distances to reach the ACE-ASIA observation locations. The USGS 25-category land-use data were used as the basis to locate the desert and semi-arid areas. During springtime in this region, additional land-cover regions such as grasslands can be seasonal dust sources (i.e., when they are not snow covered and before the grass emerges). These aspects were included in this study. In this analysis dust was modeled in two bins: sub-micron (diameter < 1μm) and super-micron (diameter > 1μm). In the dust source regions, dust was assumed to be uniformly distributed within the boundary layer.

2.3 Sensitivity studies

To investigate the dust influences, three sensitivity simulations were performed: a simulation without dust (NODUST); a simulation with dust but only considering radiative influences (NORMAL); and a simulation considering dust radiative influences and the four heterogeneous reactions (FULL). The NORMAL simulation was compared with the TRACE-P observed photolysis rates, and identified (Tang et al, 2003a). The difference between the NORMAL and NODUST cases isolates the dust influence via changing J-values. The dust influence through heterogeneous reactions is represented by the difference between the FULL and NORMAL simulations.

3. Dust distributions during the "Perfect Storm" period

During 4-14 April, a series of large dust out-breaks occurred, which were named the ACE-ASIA "perfect storm" by some researchers. Model results for this period are compared with surface weather observations and satellite images in **Figure 2**. The dust storm that appears in Figure 2A was initialized on April 5th in Northwestern China in association with a cold air outbreak and corresponding strong surface winds. Dust emitted in this event was transported to the east along the cold conveyor belt of this front, and arrived in the region of Eastern Mongolia - Northeastern China on April 7th. During this period, the dust storm intensified, as dust was continuously emitted along the cold front. This large dust storm was clearly recorded by both the GMS-5 satellite and surface weather observations. Generally the model simulation accurately captured the observed dust distribution on this day.

On April 9th (**Figure 2B**), this dust storm arrived over the Japan Sea and was moving to the northeast. Observed surface wind speeds reached 55km/h near the dust storm center. This dust-rich airmass kept moving to the east until it reached North America 4 days later. At the same time, another dust storm formed in Mongolia, also due to strong frontal winds, and moved eastward along a similar route. It should be noted that the satellite images were partially obstructed by clouds. On April 11th, the cloud and dust

distributions (**Figure 2C**) clearly reflected a warm conveyor belt of the front extending from Shanghai to Northern Japan. Again the simulated dust distribution captured the general features of this storm. The second dust-rich airmass also headed east, but its route was about 10 degree south of the previous dust storm.

The dust storms presented for these three days represent the typical situation of dust emission, transport and outflow in East Asia. Sun et al. (2001) performed a statistical analysis of Chinese dust events, and found that most dust storms are initialized due to cold air outbreaks, in association with strong frontal winds, and that the primary transport routes are usually east or southeast. The dust storms described here match this pattern.

4. Simulated dusts compared to observations

Neither the satellite nor the surface weather stations can provide quantitative information on the mass loadings associated with the dust storms. During this monsoon season, satellite observations are strongly affected by clouds. As shown in **Figure 2B**, the dust-enhanced image takes on a blue color under cloud cover situations, and the dust intensity estimation becomes vague. In this region, other events, such as volcanic eruption and the haze weather caused by biomass burning, may also affect the satellite's sensing capability for dust. The weather reports issued by the surface observatories are highly dependent on the observer's personal experiences, and by the spatial distribution of the observation sites. The difference between nighttime and daytime observations also affects the observer's judgments.

The ACE-ASIA field experiment provided measurements that allow a quantitative examination of the quality of our dust simulations. The group at the University of Hawaii (Clarke et al., this issue) on-board the NCAR C-130 aircraft measured coarse (supermicron) particles with thermo-optic aerosol discriminator (TOAD) whose evaporative temperature is higher than 300°C. These particles mainly

compose the coarse dust fraction. A density of 2.5 g/cm^3 was used to convert these particles from volume concentration to mass concentration while considering a reducing factor of 1.7 due to non-spherical particles (Clarke et al., this issue), and the results are compared with simulated coarse dust amounts for C-130 flights 4, 6 and 7 in **Figure 3**. These three flights had nearly the same flight path; i.e., the Yellow-Sea flight path as shown in **Figure 2C**. This flight path is typical of the C-130 ACE-ASIA flight routes, and comprised more than 1/3rd of the C-130 flights. Mid-visible light extinction and its components were measured at low relative humidity using nephelometers and absorption photometers (Anderson et al., this issue). These instruments operated downstream of a low-turbulence inlet on the C-130 aircraft which proved very efficient at sampling coarse-mode particles. The uncertainty of the extinction measurement during dust events is estimated to be about +/-20% (Anderson et al., this issue) and this has been confirmed by independent extinction measurements with an on-board sun-photometer (Redemann et al., 2003, this issue)

The aerosol optical extinction coefficients (AOE) for the wavelength 550nm were calculated based on Hess et al. (1998), and are also compared to the observations in **Figure 3**. To reflect uncertainties in the calculated AOE due to dust particle shape and size effects, error bars equal to 50% of modeled dust AOE are applied to **Figure 3**. For the C-130 flight 4, dust was not the main contributor to the AOE; dust accounted for less than 40% of the total AOE when the aircraft flew over Yellow Sea. On April 6th, the big dust storm existed in Eastern Mongolia - Northeastern China, and was headed to the northeast. The C-130 flight 4 encountered a remnant of an elevated dust layer from a previous dust event, which was not directly associated with the big dust storm. Under this situation, the maximum mass concentration of coarse dust (**Figure 3**) was about 90 μg/m^3 (all mass concentrations are given at standard temperature and pressure). On April 11th, the C-130 flight 6 flew in the Yellow Sea following the similar route, and encountered very high dust loadings (**Figure 2C**), identified by satellite, surface weather stations and the aircraft measurements. The coarse particle concentrations reached 2000 μg/m^3 (**Figure 3**), and the AOE

was among the highest values. For this flight, dust was the dominant contributor to the total AOE while flying over Yellow Sea. On April 12th, the 7th C-130 flight went to Yellow Sea, again following the same route. This flight encountered the remaining portion of the big dust storm. The observed coarse particle concentration and AOE were about half the values observed on the previous flight. In these three flights, the aircraft observations and simulations showed that the dust was found at altitudes lower than 4km, with the bulk of the dust concentrated at the altitudes lower than 2km.

5. Observed Aerosol Composition in Dusty and non-Dust Conditions

The model simulation provides a 4-dimensional representation of the dust distributions. The simulated dust distribution were used to classify the observation periods into non-dust and dusty categories. The model fields were used to classify the data instead of using the observations themselves, since observations of dust (and related quantities) were often missing for portions of the flights (i.e., for data completion considerations). The observation periods with simulated total dust greater than 100 $\mu g/m^3$ were defined as the dusty periods, and those with simulated total dust lower than 1 $\mu g/m^3$ as the non-dust cases. Using this classification the C-130 observations were resampled for C-130 flights 2 to 17, and divided into these two groups. Here we exclude the flight segments east of longitude 130E to avoid the disturbance of volcanic SO_2 emissions. Since the ACE-ASIA period had very frequent dust encounters, the non-dust events had fewer data points than the dusty events. **Figure 4** shows five observed correlations that have significant differences during dust and non-dust events. The aerosol composition data used in **Figure 4** are those taken using the PILS instrument (Lee et al., this issue). These data represent ions associated with aerosols less than 1.2 microns in diameter.

Dust contains relatively abundant amounts of silicon and calcium. There was a strong correlation between silicon and calcium for all observations, and the slope was constant between the two groups (not shown). This implies that the soils in East Asia contain a similar mixing ratio of calcium to silicon. Dust is the

main contributor to AOE during dust events, so **Figure 4A** shows a high correlation between AOE and fine calcium for the dusty cases. There is nearly no correlation between AOE and sub-micron Ca during non-dust events, as optical depths are dominated by BC, OC and/or sulfate under these conditions. **Figure 4B** shows the correlations between sub-micron Ca and sub-micron Mg. The dust events have a higher sub-micron ΔCa/ΔMg ratio than the non-dust events. Here Δ represents the difference between observed and background concentrations, and the background concentrations tend to be zero for most aerosol ions, but not for CO (**Figure 4E, 4F**). The value of this ratio for dust events reflects the composition ratio in the soils of the dust source regions. The Ca and Mg in the non-dust events comes from other sources, such as sea salt, which has a much lower amount of Ca relative to Mg.

A strong correlation between sulfate and ammonium is found in both dust and non-dust events. The slope of 0.34 in **Figure 4C** suggests that $(NH_4)_2SO_4$ is the dominant form for of sub-micron sulfate and sub-micron ammonium during dust events. During the non-dust events, the $\Delta NH_4^+ / \Delta SO_4^{2-}$ mass ratio was reduced to 0.099. This very low mass ratio was measured when the aircraft encountered the Shanghai plume on April 30th (C-130 flight 16). It should be noted that the observed $\Delta NH_4^+ / \Delta SO_4^{2-}$ ratio in the dust source regions was even higher. Zhang et al. (2002) found this ratio to vary from 0.66 to 1.63 in the south edge of the Loess Plateau during springtime. In fact, some of dust sources, are not deserts, but are fertilized agricultural lands. In China, carbamide, NH_4HCO_3, NH_4NO_3, and NH_4Cl are the prevailing nitrogenous fertilizers. When the dry weather during springtime converts these lands into seasonal dust sources, these volatile compounds enter the atmosphere along with dust and begin releasing ammonia gas on the dry and alkaline dust surface. During the dust transport journey, this procedure could continue. At the same time, SO_2 emitted from various sources can be converted to sulfate, either in the gas phase, or on the particle, leading to an increase in the sulfate ratio. When the dust-laden airmasses arrived at the C-130 locations, the sulfate and ammonium were nearly fully neutralized in sub-micron particles. We will discuss the aerosol composition change due to dust in the future. The non-dust events, like the Shanghai

plume, had lower absolute amounts of ammonium, but high sulfate, reflecting the large anthropogenic sulfur emissions in the region.

The $\Delta NO_3^- / \Delta NH_4^+$ ratio reported by Zhang et al (2002) in the south regions of the Loess Plateau ranged from 0.56 to 1.03, which is lower than the corresponding ratios observed on the C-130 flights during dust events. This result implies that nitrate concentrations increased during the dust transport process. This is expected as dust interactions can lead to increased amounts of particulate nitrate by providing heterogeneous reaction pathways for the conversion of NO_2 to particulate nitrate, and by providing pathways for nitric acid to partition into particulate nitrate (on calcium rich particles) (Song and Carmichael, 2001). It is interesting to note that this is true for the sub-micron particles shown here, and for the coarse mode particles (not shown). This is discussed in more detail later.

Most of the dust events encountered by the C-130 were over the Yellow Sea, which is surrounded by heavy populated areas, including 3 cities with population over 10 million: Beijing, Tianjing and Seoul. These regions emit large amounts of pollutants. During dust outflow into the Yellow Sea, dust is mixed with anthropogenic pollutants and ammonium emitted from agricultural lands. Using CO as an indicator of anthropogenic pollutants, a correlation analysis of CO with the ions was performed. The $\Delta SO_4^{2-} / \Delta CO$ ratio is shown in **Figure 4E.** The sub-micron sulfate shows 2 distinct groupings with CO. The dusty cases have a lower $\Delta SO_4^{2-} / \Delta CO$ slope because some sulfates were deposited on the coarse-dust surfaces, and not captured by the PILS instrument. The non-dust cases show a large number of points with much lower sub-micron sulfate levels. Both dusty and non-dust datasets have points where sulfate values increase independently of CO. Nitrate is more sensitive to dust than sulfate. The dominant final chemical product of SO_2 is nearly always sulfate, but the products from NO_x are relatively complex, which could be nitrate, HNO_3, RNO_3, PAN, MPAN and other gas-phase NO_y species, depending on the situations. Nitrate is not always the main NO_x product. The relationship of sub-micron nitrate versus CO is distinctly

different for the dusty and non-dust cases (**Figure 4F**). For dusty conditions nitrate levels are high, and show a strong correlation with CO, implying that nitrate could be the main NO_x product in dusty airmasses. The high dust cases tend to be associated with strong continental outflow conditions, and these air masses have often been recently mixed with freshly emitted pollutants (especially for the observations in the Yellow Sea). The non-dust cases have much lower values of nitrate.

It is important to note that the PILS data does not show a strong correlation between aerosol calcium and nitrate. This is also the case for the calcium and nitrate measured by TAS (total aerosol sampler) and MOI (micro-orifice impactor) . The lack of the correlation in the ACE-ASIA data suggests that calcium does not control the amount of aerosol nitrate. As discussed above, the total amount of nitrate is determined by the amount of anthropogenic nitrate arising from NO_x emitted from the industrial regions that mixes with the dust during the transport process.

6 Dust Influences during the C-130 Flight 6

The C-130 flight 6 is an excellent case to look for effects due to dust. As shown in **Figure 5**, on this day dust concentrations were very high, and the dust-rich air was well mixed with the pollutants. **Figure 5A** shows the observed aerosol composition in the sub-micron aerosols as measured by the PILS instrument (Lee et al., this issue). Elevated levels of sub-micron ammonium, calcium, sulfate and nitrate extend from the surface to ~3 km. Another important enhancement is the coarse portion of non-sea salt sulfate (NSS) and nitrate measured by the MOI instrument (Barry Huebert, personal communication). The MOI measured aerosols are in two bins. The coarse/fine cut diameter is about 0.8 μm, and the upper limit for coarse particle is 10 μm diameter. The coarse fractions of nitrate and sulfate reached maximum (0.7 for nitrate, 0.5 for sulfate) around 3GMT in this flight, at the time that the dust loading a peaked (**Figure 3**). This peak dust concentration is also well represented by the MOI coarse calcium concentration, which reached a peak concentration of ~20 ug/std m^3 at 3GMT (**Figure 5A**). When the aircraft left dusty region

and began its return-to-base leg (after 5:30GMT), the sulfate and nitrate coarse fractions decreased significantly.

Also shown in **Figure 5B** are the observed absorption and scattering (Anderson et al., this issue). Below 3 km, high values of scattering were measured and this is due predominately to the high levels of dust (**Figure 3**), with contributions from sulfate and nitrate. This is largely due to the coarse mode dust as shown by the fact that the fine fraction accounts for less than 20% of the total scattering. Absorption is ~100 times smaller, and is dominated by absorptive aerosols, like black carbon. Black carbon is both in the fine mode and in the coarse mode (where it is mixed with dust) (Clarke et al., this issue). The contribution of the fine mode aerosol to absorption varies from 40 to 80%. Above 4 km, dust concentrations are significantly lower, and both scattering and absorption are dominated by the sub-micron particles.

6.1 Impacts of dust on ozone

In general the STEM-2K1 model predicts ozone with some skill. For example, when compared to all C-130 ozone observations taken in ACE-ASIA, the mean observed value below 1 km was 57.3 ppbv, while the model mean sampled along the flight paths was 59.3 ppbv; and the correlation coefficient between the modeled and observed ozone was 0.7. **Figure 6** shows the observed and simulated O_3, SO_2, CO and ethyne concentrations for flight 6. The NODUST and NORMAL simulations significantly overestimated O_3 concentrations while the aircraft flew over Yellow Sea at low altitudes (< 500m). The maximum O_3 overestimation by these two simulations is ~ 20ppbv. The O_3 difference between NODUST and NORMAL is relatively small, which suggests that the dust radiative influence is small.

The observations of CO, SO_2 and ethyne show that the outflow into the Yellow Sea at low altitudes during this period was heavily polluted, and composed of various plume like features. The modeled

values reflect the high concentrations, but do not capture the fine-structure (due in large part to model resolution (i.e., 80 km horizontal and a few hundred meters vertical resolution)). The presence of dust has few impacts on CO and ethyne concentrations, and the three simulations overlapped for the two species. Dust is shown to have a significant impact on SO_2. During the period of 3-5 GMT, NORMAL and NODUST simulations (overlapped) overestimated the SO_2 concentrations. However, when the dust heterogeneous reactions for SO_2 are included, the sulfur dioxide levels are reduced by ~30%, and the predictions are closer to the observations.

Figure 6 also shows the simulated $J[O^1D]$ (photolysis rate for the reaction $O_3 => O_2 + O^1D$) along the flight path. Although this event had a high AOE, it contained large amounts of non-dust particles as well as dust. The results for the normal case include the effects of clouds, as well as the influences due to BC, OC, sulfate, and nitrate. The net effect of all the aerosols on the photolysis rates was large, decreasing $J[O^1D]$ by ~25%. Under these conditions, the additional contribution of the dust is small. Tang et al (2003a, 2003b) discussed the aerosol radiative influence on photolysis rates and subsequent photochemical activity during TRACE-P period. Most airmasses encountered by TRACE-P flights contained a significant amount of black carbon; these aerosols were "dark", and imposed significant impacts on J-values and related chemical species. For example, the averaged single scattering albedo (SSA) measured by TRACE-P was 0.82. The SSA observed by the C-130 flight 6 over Yellow Sea was 0.96, reflecting the vast amounts of dust, sulfate and nitrate, which are highly reflective aerosols. Conant et al. (this issue) indicated that the aerosol radiative forcing efficiency at top of the troposphere during the INDOEX was on average higher than that in ACE-ASIA, because the former contained a higher fraction of black carbon. Since the additional effect of dust on photolysis rates was not large, the further radiative influence on O_3 was relatively small. These results indicate that in the model world, the heterogeneous reaction with ozone is the key mechanism accounting for the observed low ozone.

The results for OH are also shown in **Figure 6**. The NORMAL and FULL simulations have nearly the same OH concentrations, and the NODUST simulation has the highest OH. This shows that the OH concentrations are determined mainly by changes in the photolysis rates. Actually in this scenario, the O_3 concentration difference between NORMAL and FULL had a large influence on OH, but this influence was offset by other effects, mainly that due to the NO_2 reaction with dust. The airmasses encountered by the C-130 flight 6 at low altitudes over the Yellow Sea were very polluted. Under these conditions, the OH concentration was strongly affected by the concentrations of other pollutants, not solely by O_3. We will discuss this in detail below.

6.2 Analysis along trajectories

The concentrations observed by the C-130 aircraft represent the results of chemical evolution during the journey of these airmasses. To further investigate the evolution, we calculated 3-dimensional trajectories for the two segments of the C-130 flight 6 shown in **Figure 7**. These two trajectories arrived at the C130 aircraft at 2:20GMT and 3:17GMT, respectively, and we refer to these as trajectory A and B. Trajectory A started from the Gobi desert, in Western Mongolia, 3 days earlier (April 8th), and traveled at a relatively low altitude before reaching the C130 aircraft at an altitude of 180m. This path closely follows the route of the dust transport. Trajectory B began at high altitude over the Taklamagan desert, kept at altitudes higher than 2km, and arrived at the aircraft at an altitude of 2500m. The airmass along this trajectory did not encounter any appreciable dust until two days before it arrived at the C-130 aircraft. We focus first on Trajectory A, as it contain large amounts of dust, and its transport path passed at low altitudes over three megacities: Beijing, Tianjing and Qingdao. The interactions between dust and the heavy anthropogenic emissions are discussed below.

Figure 8 shows calculated concentrations extracted from the three-dimensional model results, for the three simulation cases along trajectory A. In **Figure 8A** we see that the inclusion of the heterogeneous

loss of ozone results in a continuous loss of ozone along the trajectory until the airmass reached Beijing on julian day 100 (April 10th). During this early period of trajectory A, the altitude was higher than 1.5km, and the air mass did not pick-up fresh pollutants. When the airmass reached Beijing, NO_2, NO, SO_2 and HNO_3 increased significantly (**Figure 8C, 8D, 8E, 8F**), driven by local emissions. At this point, high-concentrations of anthropogenic pollutants interacted with dust via the O_3 and NO_2 heterogeneous reactions, and O_3 and other photochemical products were determined by the response of whole photochemical system to dust loading.

6.3 Chemical reaction analysis

Table 1 lists the reactions used in the following discussions, with their internal index used in our model. We first discuss SO_2, as its chemistry is the simplest. The gas-phase SO_2 chemistry occurs mainly via the reaction $OH + SO_2 + H_2O + O_2 \rightarrow HO_2 + H_2SO_4$ (R#44 in Table 1). The radiative influence of dust by itself causes an increase in SO_2 concentrations by reducing J-values and OH. However, this influence was weak compared to the SO_2 heterogeneous reaction with dust. By the time the airmass reached the C-130 aircraft, the accumulated SO_2 heterogeneous reaction reduced SO_2 concentrations by ~ 40%. The heterogeneous loss also dominated nitric acid (HNO_3) concentrations. The uptake coefficient for nitric acid is ~100 times larger than that for SO_2. The heterogeneous reaction of dust with nitric acid resulted in the depletion of nitric acid from the gas phase and the repartitioning into particulate nitrate.

The heterogeneous influence on NO_2 is more complex than that of SO_2, because the former also includes the indirect heterogeneous influence via fast gas phase reactions such as $NO + O_3 \rightarrow NO_2 + O_2$ (R#7). Since the accumulated effect of the heterogeneous reaction with O_3 is to reduce the concentrations by more than 10 ppbv before entering the polluted region, the FULL simulation also has a lower NO_2 production rate for the reaction mentioned above. Considering this influence, and the NO_2 direct heterogeneous loss, the total heterogeneous influence on NO_2 is stronger than that for SO_2. NO_2

concentrations are decreased by 17% in the source region during the daytime (**Figure 8C**). For the same reason, the NO gas-phase loss is decreased due to lower O_3 concentrations, so the NO concentration in the FULL simulation is higher than that in other two simulations (**Figure 8D**). Dust also exerts a radiative influence on NO_x (mainly through R#1), and the net influence over the polluted region is to decrease NO_2 and increase NO. However, this influence is much weaker than the heterogeneous influence.

In this study we assumed that the NO_2 heterogeneous uptake on dust is an irreversible reaction with no recycling of NO_x. Under this condition the net heterogeneous influence is to decrease gas-phase NO_x, and decrease the ratio of NO_x to NMHC (non-methane hydrocarbons) in the polluted region. In this region ozone production is NMHC–limited, and a lowering of the NO_x/NMHC ratio causes an increase in O_3 production. This effect partly offsets the O_3 loss via the heterogeneous reaction. When the airmass passed over the highly polluted region, the dust radiative influence, represented by the difference between NORMAL and NODUST, caused a decrease in O_3 concentration of 2ppbv. It should be noted that the photolysis rate changes had little impact on O_3 concentration in the early segment of this trajectory, since this air mass had low NO_x concentrations.

The OH concentrations in **Figure 8G** also show a significant difference between clean and polluted regions. In clean regions, OH is mainly generated via the O_3 photolysis: $O_3 + h\nu \rightarrow O^1D + O_2$ and $O^1D + H_2O \rightarrow 2OH$. Because the heterogeneous reactions reduce O_3 concentrations, OH is also reduced, as shown in the early segment of the trajectory in **Figure 8F**. In polluted regions, the heterogeneous removal of NO_x and SO_2 reduces OH gas-phase loss, and offsets some of the influence of the O_3 decrease. The net heterogeneous influence is to increase OH slightly in the polluted regions. HO_2 concentrations follow a similar path (not shown). At noon of April 10, when the airmass passed over Beijing, dust decreased OH by about 12% via changing photolysis rates.

The impacts of dust on HONO are also of interest. HONO is important, as it can be a significant source of HO_x. It has been suggested that heterogeneous reactions of NO_2 on dust may produce gas phase HONO (Grassian, 2002). In this study we did not include this mechanism. However, as discussed above, the heterogeneous reaction of NO_2 results in a decrease in ambient NO_2 concentrations, but a slight increase in NO and OH concentrations in the polluted region. Since R#21 ($OH + NO \rightarrow HONO$) is the dominant source for HONO, the net effect is to increase HONO by up to 25%, and the ratio of HONO/NO_2 by an even larger amount. Our simulations showed the HONO/NO_2 ratio (**Figure 8H**) to increase by about 30%. Calvert et al (1994) suggested that the nighttime HONO production could occur via a heterogeneous process with moist aerosols. The HONO enhancement in **Figure 8H** solely reflects the response of the photochemical system to the heterogeneous removal of O_3, NO_2, HNO_3 and SO_2 in the polluted region.

Figure 8I shows the correlation of O_3 heterogeneous loss rate versus O_3 concentration difference between the FULL and NORMAL simulations along trajectory A. This correlation is relatively strong along most segments of the trajectory, and the correlation coefficient in Figure 8I is 0.88. However, when the airmass passed over the polluted areas, the correlation changed, and the O_3 loss tendency became weaker. After the airmass left this region, the amplification of O_3 difference was restored. This variation is represented in the segment where the O_3 difference ranged from 15 to 20ppbv. In the polluted region, the response of the whole photochemical system to heterogeneous reactions determined the net heterogeneous influences on O_3 and other species, and the O_3 difference was not linearly correlated to the O_3 heterogeneous loss.

6.4 Chemical process analysis

To further investigate the photochemical system in the polluted region, we performed a chemical process analysis at one point near Beijing along trajectory A. This point is located at Julian day 100.14 (near local noon) of the trajectory in **Figure 7**. **Figure 9** shows the chemical budgets of O_3, NO_2, NO and OH (OH is presented in concentration), and their main production and loss terms at this point. For the O_3 chemical

budget, the reaction with NO (R#7) is the primary loss process, and this loss rate is related to O_3 background concentrations. O_3 production comes mainly from the O^3P generated by NO_2 photolysis. The photolysis of O_3 itself also contributes to O^3P via reaction R#17, but it is not as strong as the NO_2 photolysis at this point. For reactions R#2, R#7 and R#17, the FULL simulation has the lowest reaction rate, and the NODUST has the highest (since the NODUST had the highest photolysis rates). The FULL simulation also has the lowest reaction rate for R#8: $O_3 + NO_2 \rightarrow NO_3 + O_2$, due to the lower O_3 and NO_2 concentrations. At this point, the O_3 heterogeneous loss rate on dust (R#237) was -1.4×10^{-4} ppbv/s (negative values indicate loss terms). The NORMAL simulation has a net positive O_3 chemical budget of 9.9×10^{-4} ppbv/s in **Figure 9A**. If the O_3 budget difference between FULL and NORMAL simulations solely depends on the O_3 heterogeneous reaction R#237, the O_3 net budget in the FULL would be 8.5×10^{-4} ppbv/s, but the actual value in **Figure 9A** is 8.9×10^{-4} ppbv/s. This means that the photochemical system provided an additional O_3 production rate of 4.6×10^{-5} ppbv/s to offset part of the O_3 heterogeneous loss at this point.

In polluted regions, most of the NO_x comes from surface emissions. The strongest net heterogeneous influence on NO and NO_2 occurred in the early morning instead of at noontime. At 8:50 LST, April 10, the NO_2 budget difference between FULL and NORMAL simulations was -4.5×10^{-5} ppbv/s, and the NO_2 heterogeneous loss rate was -3.8×10^{-5} ppbv/s. At that time, the NO budgets for FULL and NORMAL simulations were 1.471×10^{-5} and 1.458×10^{-5} ppbv/s, respectively. At the early morning O_3 concentrations were strongly affected by the NO_x thermal reactions, and the lower O_3 concentrations in the FULL simulation caused an additional NO_2 decrease (other than the reaction R#236), and enhanced the NO concentration. At the time shown in **Figure 9** (about 11:20 LST), the NO_2 and NO differences between these two simulations were 0.8 and 0.3 ppbv, respectively. However, these differences did not continue to increase, but instead narrowed as the photolysis rates reached their daily maximum. At 11:20LST, the reactions R#1 and R#7 became the main terms for the NO and NO_2 budgets (**Figure 9B, 9C**), and the

reaction R#31: $HO_2 + NO \rightarrow OH + NO_2$ ranked third. R#31 is important for O_3 production because it generates additional NO_2. R#21 is the main reaction for HONO production. The FULL simulation had the highest reaction rates for these two reactions (**Figure 9A, 9B**). However, for another much faster reaction R#25: $NO_2 + OH \rightarrow HNO_3$, the FULL had the lowest reaction rate (**Figure 9B, 9D**). So the FULL simulation had the lowest OH loss for the reactions with NO_x. At this time, NO_x was mainly removed through photochemical gas-phase reactions, and the influence of the NO_2 heterogeneous reaction R#236 on NO_x budget at this time was not as important as that at early morning or night.

Figure 9D shows OH concentrations, and their loss and production terms at 11:20LST. We did not list the numerous reactions between OH and hydrocarbons, and their products in **Figure 9D**, but these reactions accounted for the OH concentrations in this figure. As a short-lived radical, OH concentration is determined by its local budget. R#19 is the main source of OH in low NO_x regions, and is primarily determined by photolysis rates and O_3 concentration. This reaction rate varied from fastest to slowest in the following way: NODUST > NORMAL > FULL. The difference between NODUST and NORMAL is mainly due to differences in the $J[O^1D]$ rates, and the FULL case had the lowest because it had the lowest O_3 concentration. At this time, the main OH producing reaction was not R#19, but R#31. Among the three simulations, FULL had the highest reaction rate for R#31. R#22: $HONO + hv \rightarrow OH + NO$ was also important at this time. Here HONO plays an important role in the HO_x budget, because the photolysis reaction: $HONO + hv + O_2 \rightarrow HO_2 + NO_2$ is a source for HO_2, and HO_2 can contribute to OH production via R#31. The FULL simulation had the highest HONO concentration. The product of R#25, HNO_3, can also be renoxificated via its photolysis reaction: $HNO_3 + hv \rightarrow OH + NO_2$, but this photolysis rate is about 3 orders of magnitude smaller than the HONO photolysis rate (R#22).

The chemical variations along trajectory B in **Figure 7** are relatively simple. This trajectory kept an altitude higher than 2km for the whole journey, and encountered few fresh pollutants. This airmass encountered dust 2 days before it arrived at the C-130 aircraft. As a consequence, the dust influences along this trajectory were weaker than those along trajectory A. **Figure 10A** shows the O_3 concentrations and O_3 heterogeneous loss along the trajectory B. The dust radiative influence was small. Since there were very low concentrations of pollutants, the impact of heterogeneous reactions of SO_2 and NO_2 were also small. The O_3 heterogeneous reaction is still important. However, this reaction was also much weaker than that along trajectory A due to the difference of their dust concentrations. When this airmass arrived at the C-130 aircraft, the accumulated O_3 loss on dust led to an O_3 difference of ~ 13. **Figure 10B** shows the correlation between O_3 heterogeneous reaction and O_3 levels, and the correlation coefficient R^2 is 0.98 (higher than that in trajectory A). The slope of the best-fit line in **Figure 10B** is about twice that in **Figure 8I**, because the latter includes some impacts which can partially offset O_3 heterogeneous loss.

These results suggest that heterogeneous reactions involving dust and ozone can be important. Quantifying the role of this reaction in the field is challenging, as the ozone reaction with dust leaves no obvious signature on the aerosol surface. Thus at present we must rely on inferring its importance from changes in ambient levels of ozone.

6.5 Implications for sulfate and nitrate

As discussed above SO_2, NO_2 and HNO_3 also can react with dust surfaces. In this case, these reactions should result in increased amounts of sulfate and nitrates in the aerosol, and a change in the size distributions of these components. The sulfate and nitrate formed via ordinary nucleation should concentrate in the accumulation mode if the aerosol concentrations are not very high. The presence of dust changes this pattern. As discussed in Song and Carmichael (2001), the surface reactions involving these species should increase the super-micron amounts of sulfates and nitrates. The ACE-ASIA

observations support this hypothesis. As shown in Figure **5A**, during high dust loading periods (e.g., 3GMT in C-130 flight 6) there were high coarse portions for sulfate (0.51) and nitrate (0.68). During the low dust events at 6GMT, the coarse fractions were very small (< 0.08). Comparing these two segments, the surface reactions on dust show significant impacts. As shown in **Figure 8** and discussed above, the SO_2 surface reaction with dust increased the sulfate production by ~30%, and due to surface area considerations, most of this occurred in the coarse fraction.

The reaction of nitric acid with dust is much faster than the SO_2 reaction, and will proceed until all the carbonate in the aerosol (in the case of $CaCO_3$ particles) is consumed (Kruger et al., 2003). This procedure is mainly limited by the availability of HNO_3. If HNO_3 supply is sufficiently large, nitrate is expected to be closely associated with calcium in the aerosol, both in terms of amount and in terms of size distribution. **Figure 5A** shows that the nitrate coarse fraction is more sensitive to dust than that of sulfate. During the low-dust periods (around 6GMT in C-130 flight 6), the nitrate coarse fraction was ~ 0.01, and it was 0.7 during the heavy dusty event (3GMT). This fraction change is bigger than that for the sulfate coarse fraction, which reflects HNO_3's faster heterogeneous uptake.

7. Regional Dust Influences

Figure 11 shows the averaged dust radiative influences on O_3 and daytime OH during the period 4 –14 April 2001. OH is one of the most sensitive species to photolysis rate changes. Averaged daytime OH decreased up to 20% for the layer below 1km, and the strongest decrease occurred in Northeastern China and the Japan Sea. For the layer from 1 to 3km, the radiative influence on OH has a similar distribution pattern to that in the lower layer, but a lower intensity. The dust radiative impact on O_3 is also affected by the pollutant concentrations. In polluted areas that were impacted by the dust storms, such as Northeastern China, O_3 concentrations decreased because dust reduced the photochemical O_3 production. For the layers below 1km and 1~3km, the O_3 decrease was less than 1%, and much weaker than that for OH. O_3

concentrations also increased in low-NO_x regions, such as Taklamagan desert, due to decreased O_3 photolytic loss. O_3 enhancement for the layer below 3km is weak (< 0.2%). In the layer above 3km, dust radiative influence on O_3 is larger. Due to photolysis enhancement over the Taklamagan desert and part of Mongolia, O_3 concentrations decreased up to 5%. O_3 concentrations increase up to 0.5% in some places due to the accumulated impacts of low O_3 photolytic losses. In contrast, dust heterogeneous influence on O_3 is much stronger than its radiative influence, especially near the surface.

Figure 12 shows that the averaged O_3 decrease due to the heterogeneous reactions is as large as 20% for the layer below 1km. This O_3 heterogeneous decrease is up to 15% for the layer from 1 to 3km, and 6% for the layer above 3km. The distribution of O_3 decrease due to heterogeneous reaction is similar to the dust distribution, except in polluted regions. As we discussed previously, in the polluted regions, the complex response of photochemical system to the heterogeneous reactions can offset part of the O_3 heterogeneous loss. The distribution of SO_2 decrease is similar to that of O_3 in **Figure 12**. On averaged SO_2 is decreased by up to 55%, and is solely caused by its heterogeneous loss on dust. The HNO_3 decrease in **Figure 12** is also due to the corresponding heterogeneous reaction with dust, but its impact is much larger (up to 95%), and the area is much bigger than that of SO_2. The NO_2 decrease is much smaller than the SO_2 reduction (up to 20% below 1km). Moreover, the distribution of NO_2 decrease is not as broad as that of SO_2. In some places, such as Shanghai and Tokyo plumes, the NO_2 concentrations are increased by 2%-6%. Due to the extensive O_3 decrease after considering the heterogeneous reactions, the NO_2/NO ratio decreased, and NO_2 is converted to NO, leading to the corresponding NO enhancement. The NO_2 decrease also caused a decrease in secondary products, such as PAN. However, total NO_x was not decreased under this circumstance because more NO_x was stored as NO. In fact, the NO_x consumption was reduced, and the net impact of the above conversions led to NO_2 enhancement due to the NO-NO_2 fast balance in the downwind sites of strong sources, if the NO_2 heterogeneous loss is smaller than the reduction in the photochemical loss.

Figure 13 shows that NO increased in most regions due to dust heterogeneous influences, and this enhancement can be up to 20%. However, in some clean areas, the NO_2 heterogeneous loss has a more significant impact on NO than the O_3 heterogeneous loss. In these areas, the NO_2 heterogeneous loss is very important to the total NO_x budget, and caused the NO concentration to decrease by up to 10%. The area distribution of the HONO change can be explained by the NO variation, and HONO changed from –6% to 30% for the layer below 1km. As a short-lifetime radical, OH concentration mainly reflects its local chemical budget. In clean areas, the OH concentrations were reduced by up to 10% due to O_3 heterogeneous loss. OH concentrations did not change much in most polluted areas, and slightly increased (up to 4%) in the large cities where the dust storms passed. As we discussed in the last section, the OH increase reflected the complex response of photochemical system to the dust heterogeneous reactions with O_3 and NO_2.

Figure 13 also shows that dust enhances sulfate by up to 25% below 1km, when averaged in this period. This sulfate enhancement is mainly due to the SO_2 heterogeneous reaction with dust. If no dust exists, the sulfate formed from ordinary SO_2 oxidization and nucleation is usually concentrated in fine or accumulative mode, and coarse sulfate should be very limited. SO_2 uptake on dust surfaces should create sulfate on dust surface, and the size distribution of this sulfate enhancement depends on the dust size distribution and surface size. Because dust contains higher coarse portion than the ordinarily formed sulfate particle, dust appearance generally leads to increase the sulfate coarse portion (Song and Carmichael, 2001). In the locations where the C-130 flew, the average effect on sulfate was on the order of 10%. The size distribution of sulfate has important implications for climate forcing. Sulfate in the coarse mode has a much smaller impact on the planetary radiative balance than fine-mode sulfate. Fine-mode sulfate scatters vastly more solar radiation, has a much longer atmospheric lifetime, and has the potential to influence cloud-droplet number. The results for this high dust loading period may represent an

upper limit estimate for the impact of dust. However, these results are based on a simplified treatment of the heterogeneous chemistry. While these results are generally consistent with the C-130 aircraft observations, further efforts in terms of modeling and observations are needed before this fraction can be better quantified.

The dust heterogeneous influences eventually decrease along with the increase of altitude and decrease of dust and pollutant loadings. These influences can be transported or diffused to high altitudes, depending on the weather situation. Dust heterogeneous influences on most chemical species except OH are stronger than corresponding radiative influences for layer lower than 3km. During the "perfect storm" period, the dust influences covered extensive areas.

7. Summary

The distribution of dust, its composition, and its influences on gas-phase chemistry during 4-14 April 2001, was studied using a comprehensive regional transport model, STEM, and the ACE-ASIA C-130 aircraft measurements. Simulated dust was shown to capture many of the important features observed by the surface weather reports, satellite images, and the C-130 aircraft observations. The dust generation accompanied cold air outbreaks and the associated strong frontal winds. During this period, dust storms were initialized in the Taklamagan and Gobi deserts, and transported eastward. Along the transport routes, dust loadings were enhanced by dust emissions in from Loess Plateau region, and exposed agricultural lands. The STEM-simulated coarse dust concentrations were compared with the C-130 observations of coarse particles inferred from refractory volumes of the coarse mode. Calculated values of extinction were also compared to aircraft observations. The model was shown to capture many of the important observed features, including the variations along the C-130 flights 4, 6 and 7. During this period, dust was the dominant contributor to AOE. Using the simulated dust to resample the airmasses encountered by the C-

130 flights, and to divide them into dust and non-dust events, the dusty air-masses were shown to have elevated values of $\Delta Ca/\Delta Mg$, $\Delta NH_4^+ / \Delta SO_4^{2-}$, and $\Delta NO_3^-/\Delta CO$.

Dust influences on regional gas-phase chemistry can be classified into heterogeneous influences and radiative influences, and both were studied. In this paper we introduced four heterogeneous reactions involving O_3, NO_2, SO_2 and HNO_3 reactions on dusts. The C-130 flight 6 was significantly affected by heterogeneous and radiative influences. The O_3 heterogeneous uptake on dust had a significant impact on flight 6, accounting for a 20 ppbv decrease in ozone levels. Only when this reaction was included in the model were we able to represent the observed values. This reaction was shown to cause a broad decrease in background O_3. In polluted areas, this low O_3 background reduced NO_2 production, but caused NO enhancement. The impact of the O_3 heterogeneous loss on NO_2 was usually stronger than that due to the direct NO_2 reaction on dust. As a result of these reactions HONO levels increased by up to 30% in some polluted areas. The radiative influence of dust on photochemistry was largest for HO_x. For ozone, radiative influence of aerosols was large, but the contribution due to dust was not as strong as the influences of the heterogeneous reactions.

The presence of dust was also shown to enhance sulfate production by 10 to 40% in dust rich regions, and to result in an increase in the sulfate mass in the coarse fraction. The observational data also found similar amounts of coarse mode-sulfate. A pathway for producing coarse-mode sulfate has important implications for climate. Sulfate in the coarse-mode has a much weaker influence on radiative forcing than sulfate in the fine-mode. Sulfate-on-dust, in comparison with sulfate-in-accumulation mode, scatters vastly less solar energy, has a much shorter atmospheric life-time, and has a smaller impact on cloud-droplet number. The results presented here provide an upper-limit estimate of the importance of this reaction pathway, since the evaluation was done under high-dust load conditions. For individual events, as much as 30-40% of the sulfate was found in the coarse-mode. When averaged over the 10 day period encompassing the

life-cycle of this large dust outbreak, 10-15% of sulfate was predicted in the coarse-mode over vast regions downwind of the high sulfur emission regions of east Asia.

Reactions involving NO_2 and nitric acid were shown to result in the accumulation of nitrate into the aerosol, and this occurs mainly in the coarse mode (however, appreciable amounts may also appear in the fine mode).

Clearly further work is needed to quantify the influences of dust in the photochemical and biogeochemical cycles in East Asia. The heterogeneous reactions as modeled were very simple. More detailed considerations of the possible effects of surface saturation, as well as competition for reactions on other surfaces such as BC need to be considered. These effects, as well as a comprehensive comparison of across the ACE-ASIA measurements are the subjects of a future paper.

These results also point out the challenges that the community faces in quantifying the impacts of aerosols on the chemistry of the atmosphere. For example, the results presented here strongly suggest that heterogeneous reactions involving dust and ozone can be important. However, quantifying the role of this reaction in the field is challenging, as the ozone reaction with dust leaves no obvious signature on the aerosol surface confirming that the reaction indeed occurred. Thus at present we must rely on inferring its importance from changes in ambient levels of ozone, which requires de-convoluting the heterogeneous reaction signal from competing gas-phase photochemical destruction/production reactions, along with transport and deposition processes.

Furthermore the evaluation of the importance of heterogeneous reactions involving dust requires quantification of the dust amount, its size and surface area distributions in space and time, and its elemental composition. Of particular importance in understanding the mechanisms of these heterogeneous

reactions, and in evaluating our capabilities of modeling the phenomena, is the quantification of the chemical composition of the aerosol over the entire size range that dust exists in the atmosphere. The observations obtained during ACE-ASIA have produced the most comprehensive characterization of dust to date. For example, the data on board the C-130 on dust mass (estimated from the refractory portion of super-micron optical size distribution), mid-visible, low-RH light extinction by aerosols, along with aerosol chemical composition data provided by PILS, TAS and MOI, discussed in this paper provide valuable new information that imply and confirm aspects of the nature of the dust/pollution interactions in the East Asia troposphere. However, the integration of these observations into a consistent data set that can be used to quantify important aspects of dust pollution interaction (for example the amount of non-sea salt sulfate in the coarse mode), and that can be used to test and constrain models remains a challenge. Uncertainties in aspects of the observations (e.g., converting optical quantities to mass (associated with composition and shape effects), and differences in the amount of information (for example temporal resolution) on the chemical composition of the coarse and fine modes, provide ample opportunity for the model, with over-simplified treatments of aerosol interactions, to "agree" with the observations. A closer integration of the measurements and models, and the identification of additional indicators of dust/chemistry interactions that can be used to more rigorously test/constrain models are needed.

Acknowledgements:

This work was supported in part by grants from the NSF Atmospheric Chemistry Program, NSF grant Atm-0002698, NASA GTE and ACMAP programs, and the Department of Energy Atmospheric Chemistry Program. This work (I. Uno) was also partly supported by Research and Development Applying Advanced Computational Science and Technology (ACT-JST) and the CREST of Japan Science and Technology Corporation.

Reference:

Anderson, T. L., S. J. Masonis, D. S. Covert, N. C. Ahlquist, S. G. Howell, A. D. Clarke, and C. S. McNaughton, Variability of aerosol optical properties derived from in situ aircraft measurements during ACE-Asia, *J. Geophys. Res.*, *10.1029/2002JD003247*, this issue.

Calvert, J. G., G. Yarwood, and A. M. Dunker, An evaluation of the mechanism of nitrous-acid formation in the urban atmosphere, *Research on Chemical Intermediates*, 20 (3-5): 463-502, 1994.

Carter, W., Documentation of the SAPRC-99 chemical mechanism for voc reactivity assessment, Final Report to California Air Resources Board Contract No. 92-329, University of California-Riverside, May 8, 2000

Carmichael, G. R., Y. Tang, G. Kurata, I. Uno, D. G. Streets, J.- H. Woo, H. Huang, J. Yienger, B. Lefer, R. E. Shetter, D. R. Blake, A. Fried, E. Apel, F. Eisele, C. Cantrell, M. A. Avery, J. D. Barrick, G.W. Sachse, W. L. Brune, S. T. Sandholm, Y. Kondo, H. B. Singh, R. W. Talbot, A. Bandy, A. D. Clarke, and B. G. Heikes, Regional-Scale chemical transport modeling in support of intensive field experiments: overview and analysis of the TRACE-P Observations, *J. Geophys. Res.*, *10.1029/2002JD003117*, 2003.

Clarke, A. D., Y. Shinozuka, V.N. Kapustin, S. Howell, B. Huebert, S. Masonis, T. Anderson, D. Covert, R. Weber, J. Anderson, H. Zin, K.G. Moore II, and C. McNaughton, Size-distributions and mixtures of black carbon and dust aerosol in Asian outflow: physio-chemistry, optical properties, and implications for CCN, (submitted to *J. Geophys. Res.*, this issue).

Conant, W. C., J. H. Seinfeld, J. Wang, G. R. Carmichael, Y. Tang, I. Uno, P. J. Flatau, K. M. Markowicz, and P. K. Quinn, A model for the radiative forcing during ACE-Asia derived from CIRPAS Twin Otter and R/V Ronald H. Brown data and comparison with observations, *J. Geophys. Res.*, this issue (in press).

Dentener, F. J., G. R. Carmichael, Y. Zhang, J. Lelieveld, and P. J. Crutzen, Role of mineral aerosol as a reactive surface in the global troposphere, *J. Geophys. Res.,* 101, 22869-22889, 1996.

Goodman, A. L., G. M. Underwood, and V. H. Grassian, A laboratory study of the heterogeneous reaction of nitric acid on calcium carbonate particles, *J. Geophys. Res.,* 105, 29053-29064, 2000.

Goodman, A. L., P. Li, C. R. Usher, and V. H. Grassian, Heterogeneous uptake of sulfur dioxide On aluminum and magnesium oxide particles, *J. Phys. Chem. A*, *105,* 6109-6120, 2001.

Grassian, V. H. , Chemical reactions of nitrogen oxides on the surface of oxide, carbonate, soot and mineral dust particles: Implications for the chemical balance of the troposphere, *J. Phys. Chem. A, 106*, 860-877, 2002.

Hanisch, F. and J. N. Crowley, Heterogeneous reactivity of gaseous nitric acid on Al_2O_3, $CaCO_3$, and atmospheric dust samples: A Knudsen cell study, *J. Phys. Chem. A*, 105, 3096-3106, 2001.

Hess, M., P. Koepke, and I. Schult, Optical properties of aerosols and clouds: the software package OPAC, *Bulletin of the American Meteorological Society*, 79(5), 831-844, 1998.

Huebert, B. J., T. Bates, P. B. Russell, G. Shi, Y. J. Kim, K. Kawamura, G. R. Carmichael, and T. Nakajima, An overview of ACE-ASIA: strategies for quantifying the relationships between Asian aerosols and their climatic impacts. (submitted to *J. Geophys. Res.,* this issue).

Jacob, D. J., Heterogeneous chemistry and tropospheric ozone, *Atmos. Environ.*, 34, 2131-2159, 2000.

Jordan, C. E., J. E. Dibb, B. E. Anderson , and H. E. Fuelberg, Uptake of nitrate and sulfate on dust aerosols during TRACE-P. (submitted to *J. Geophys. Res.,* TRACE-P issue), 2003.

Krueger, B. J., V. H. Grassian, A. Laskin, and J. P. Cowin, The transformation of solid atmospheric particles into liquid droplets through heterogeneous chemistry: laboratory insights into the processing of calcium containing mineral dust aerosol in the troposphere, submitted to *Geophys. Res. Letts.*, *30,* 48-1 to 48-4. (*DOI 10.1029/2002GL016563*), 2003.

Lee, Y. N., R. Weber, Y. Ma, D. Orsini, K. Maxwell, D. Blake, S. Meinardi, G. Sachse, C. Harward, T. Anderson, S. Masonis, A. D. Clarke, K. Moore, V. N. Kapustin, T.-Y. Chen, D. C. Thornton, F. H. Tu, and A. R. Bandy, Airborne measurement of inorganic ionic components of fine aerosol particles using the PILS-IC technique during ACE-ASIA and TRACE-P. (submitted to *J. Geophys. Res.*, this issue).

Liu, M. and D. L. Westpal, A study of the sensitivity of Simulated mineral dust production to model resolution, J. Geophys. Res., 106 (D16), 18099-18112, 2001.

Madronich, S. and S. Flocke, The role of solar radiation in atmospheric chemistry, in *Handbook of Environmental Chemistry* (P. Boule, ed.), Springer-Verlag, Heidelberg, 1-26, 1999.

Madronich, S., photodissociation in the atmosphere 1: actinic flux and the effects of ground reflections and clouds, *J. Geophys. Res.*, 92(D8), 9740-9752, 1987.

Monahan, E. C., D. E. Spiel, and K. L. Davidson, Amodel of marine aerosol generation via whitecaps and wave disruption, *Oceanic Whitecaps* edited by E. C. Monahan and G. MacNiocaill, 167-174, D. Reidel, Norwell, Mass., 1986.

Michel, A. E., C. R.Usher, and V. H. Grassian, Heterogeneous and catalytic uptake of ozone on mineral oxides and dust: a knudsen cell investigation, *Geophys. Res. Letts.*, *29,* 10-1 to 10-4, 2002.

Phadnis, M. J., and G. R. Carmichael, Influence of mineral aerosol on the tropospheric chemistry of east Asia, *J. Atmos. Chem., 36,* 285-323, 2000.

Prince, A. P., J. L. Wade, V. H. Grassian, P. D. Kleiber, and M. A Young, Heterogeneous reactions of soot aerosols with nitrogen dioxide and nitric acid studied in an atmospheric chamber, *Atmos. Environ.*, *36*, 5729-5740, 2002.

Redemann, J., S. J. Masonis, B. Schmid, T. L. Anderson, P. Russell, J. Livingston, A. Clarke, S. Howell, and C. McNaughton, Clear-column closure studies of aerosol extinction and optical depth aboard the NCAR C-130 in ACE-Asia, 2001. (submitted to *J. Geophys. Res.*, this issue).

Song, C. H., and G. R. Carmichael, A three-dimensional modeling investigation of the evolution processes of dust and sea-salt particles in east Asia, *J. Geophys. Res., 10*6, 18,131-18, 154, 2001.

Streets, D. G., T.C. Bond, G. R. Carmichael, S. D. Fernandes, Q. Fu, D. He, Z. Klimont, S. M. Nelson, N. Y. Tsai, M. Q. Wang, J.-H. Woo, and K. F. Yarber, A year-2000 inventory of gaseous and primary aerosol emissions in Asia to support TRACE-P modeling and analysis (submitted to *J. Geophys. Res.,* TRACE-P issue), 2003.

Sun, J., M. Zhang, and L. Tungsheng, Spatial and temporal characteristics of dust storms in China and its surrounding regions, 1960-1999: Relations to source area and climate, *J. Geophys. Res., 10*6, 10325-10333, 2001.

Tang, Y., G. R. Carmichael, I. Uno, J.-H. Woo, G. Kurata, B. Lefer, R. E. Shetter, H. Huang, B. E. Anderson, M. A. Avery, A. D. Clarke and D. R. Blake, Impacts of aerosols and clouds on photolysis frequencies and photochemistry during TRACE-P, part II: three-dimensional study using a regional chemical transport model, *J. Geophys. Res.*, *10.1029/2002JD003100*, 2003a.

Tang, Y., G. R. Carmichael, J.-H. Woo, N. Thongboonchoo, G. Kurata, I. Uno, D. G. Streets, D. R. Blake, R. J. Weber, R. W. Talbot, Y. Kondo and H. B. Singh, the influences of biomass burning during TRACE-P experiment identified by the regional chemical transport model, *J. Geophys. Res.*, *10.1029/2002JD003110*, 2003b.

Underwood, G. M., C. H. Song, M. Phadnis, G. R. Carmichael, and V. H. Grassian, Heterogeneous reactions of NO_2 and HNO_3 on oxides and mineral dust: A combined laboratory and modeling stud*y, J. Geophys. Res., 10*6, 18,055-18,066, 2001.

Uno, I., G. R. Carmicahel, D.G. Streets, Y. Tang, J. J. Yienger, S. Satake, Z. Wang, J.-H. Woo, S. Guttikunda, M. Uematsu, K. Matsumoto, H. Tanimoto, K. Yoshioka and T. Iida, Regional Chemical Weather Forecasting System CFORS: Model descriptions and analysis of surface observations at Japanese island stations during the ACE-ASIA experiment. (submitted to *J. Geophys. Res.*, this issue).

Usher, C. R., H. Al-Hosney, S. Carlos-Cuellar, and V. H. Grassian, A laboratory study of the heterogeneous uptake and oxidation of sulfur dioxide on mineral dust particles, *J. Geophys. Res.*, 107 (D23): art. no. 4713, 2002,

Wang, T., A. J. Ding, D. R. Blake, W. Zahorowski, C. N. Poon, and Y. S. Li, Chemical Characterization of the Boundary Layer Outflow of Air Pollution to Hong Kong during February- April 2001, (submitted to *J. Geophys. Res.*, TRACE-P issue), 2003.

Woo, J.-H., D. G. Streets, G. R.Carmichael, Y. Tang, B.-I. Yoo, W.-C. Lee, N. Thongboonchoo, S. Pinnock, G. Kurata, and I. Uno, Biomass and Biofuel Emissions and Their Impact on Trace Gas Distributions in Asia during the TRACE-P Experiment**,** *J. Geophys. Res., 10.1029/2002JD003200,* 2003.

Zhang, X. Y., J. J. Cao, L. M. Li, R. Arimoto, Y. Cheng, B. Huebert, and D. Wang, characterization of atmospheric aerosol over XiAn in south margin of Loess Plateau, China, *Atmos. Environ.*, 26, 4189-4199, 2002.

Zhang, Y. and G. R. Carmichael, The role of mineral aerosol in tropospheric chemistry in East Asia – A model study, *J. Apply. Meteoro.*, 38, 353-366, 1999.

Table 1. Reaction index as mentioned in Figure 9.

Reaction Index #	Reaction Equations
1	$NO_2 + hv \rightarrow NO + O^3P$
2	$O^3P + O_2 \rightarrow O_3$
7	$O_3 + NO \rightarrow NO_2 + O_2$
8	$O_3 + NO_2 \rightarrow NO_3 + O_2$
9	$NO + NO_3 \rightarrow 2NO_2$
17	$O_3 + hv \rightarrow O_2 + O^3P$
18	$O_3 + hv \rightarrow O_2 + O^1D$
19	$O^1D + H_2O \rightarrow 2OH$
21	$OH + NO \rightarrow HONO$
22	$HONO + hv \rightarrow OH + NO$
25	$OH + NO_2 \rightarrow HNO_3$
29	$OH + CO + O_2 \rightarrow HO_2 + CO_2$
30	$OH + O_3 \rightarrow HO_2 + O_2$
31	$HO_2 + NO \rightarrow NO_2 + OH$
32	$HO_2 + NO_2 \rightarrow HNO_4$
41	$H_2O_2 + hv \rightarrow 2OH$
44	$OH + SO_2 + H_2O + O_2 \rightarrow H_2SO_4 + HO_2$
125	$OH + HCHO \rightarrow HO_2 + CO$
236	$NO_2 + Dust \rightarrow 0.5Nitrate + 0.5\ Nitrite$
237	$O_3 + Dust \rightarrow 1.5O_2$

Figure Captions:

Figure 1. STEM schematic for considering the aerosol impacts on photolysis rates as well as heterogeneous chemistry.

Figure 2. Dust storms shown by the model simulation, surface synoptic observation, and GMS-5 satellite images (dust enhanced) at 06GMT (about 14:00 local time) of April 7, 9, and 11. The model results (left plates) are averaged from the model layers below 3km, and dust symbols are plotted in the station locations where dust weathers were reported at those times. The path (red line) of C-130 flight 6 is shown on plot C.

Figure 3. Simulated and observed coarse dust and total aerosol optical extinction (AOE) along C-130 flights 4, 6, and 7. The modeled coarse dust concentrations are compared to the volume concentration of observed coarse particles whose evaporative temperature is higher than 300°C. The error bars in right plots are equal to 50% of modeled dust AOE, which represents the possible estimation error due to irregular dust shape and size.

Figure 4. Observed correlations among PILS sub-micron ions and CO during C-130 flights 2 to 17 for dust and non-dust events in west of longtitude130E. Dust events were defined as that modeled total dusts were higher than 100 ug/m^3 in standard state, and non-dust events were defined as that these concentrations were lower than 1 ug/m^3. The linear best-fit lines and correlation coefficients R are marked in the plots.

Figure 5. Observed aerosol compositions (A) and optical properties (B) during C-130 flight 6.

Figure 6. Observed and simulated O_3, SO_2, CO, ethyne concentrations, and simulated $J[O_3 \rightarrow O_2+O^1D]$ and OH, along the path of the C-130 flight 6 (April 11). The three simulations (NORMAL, NODUST and FULL) have the nearly same concentrations for CO and ethyne.

Figure 7. Trajectory paths that arrived at the C-130 flight path at 2:20GMT (A) (solid line) and 3:17GMT (B) (dashed line), April 11.

Figure 8. Extracted results from the three simulations along the trajectory path A in Figure 7. A) O_3 concentrations, altitude in AGL (altitude above ground level), and longitude. B) O_3 budgets and O_3 heterogeneous loss rate on dust (all loss terms are shown in negative values, same as below). C) NO_2 concentrations and NO_2 heterogeneous loss rate on dust. D) NO concentrations and the loss via reaction $NO + O_3 \rightarrow NO_2 + O_2$. E) SO_2 concentrations and SO_2 heterogeneous loss rate on dust. F) HNO_3 concentrations and HNO_3 heterogeneous loss rate on dust. G) OH concentrations. H) $HONO/NO_2$ along the trajectory path. I) O_3 difference between FULL and NORMAL simulations versus O_3 heterogeneous loss rate on dust for all the points along the trajectory A.

Figure 9. The chemical budgets and their main components for O_3, NO_2, NO, and OH when the trajectory path A (Figure 7) passed over Beijing at Julian day 100.14 (Figure 8), or 11:20 local time, April 10. Some small budgets and terms are multiplied with 10 or 100 for displaying purpose. All loss terms are presented in negative value. For each term, the bar sequence from left to right are in FULL, NORMAL and NODUST. The reaction index (R#) is listed in Table 1.

Figure 10. Extracted results from the three simulations along the trajectory path B in Figure 7. A) O_3 concentrations, altitude, and O_3 heterogeneous loss rate on dust. B) O_3 difference between FULL and NORMAL simulations versus O_3 heterogeneous loss rate on dust for all the points along the trajectory B.

Figure 11. Averaged dust influences ((NORMAL-NODUST)/NODUST×100%) on O_3 and daytime OH via changing photolysis rates, represented in percentage change, for the layers below 1km, 1 to 3km during the period from April 4 to 14.

Figure 12. Averaged dust influences ((FULL-NORMAL)/NORMAL×100%) on O_3, NO_2, SO_2, and HNO_3 below 1km via the heterogeneous reactions for the period April 4-14.

Figure 13. Same as Figure 12 but for daytime OH, NO, HONO, and sulfate.

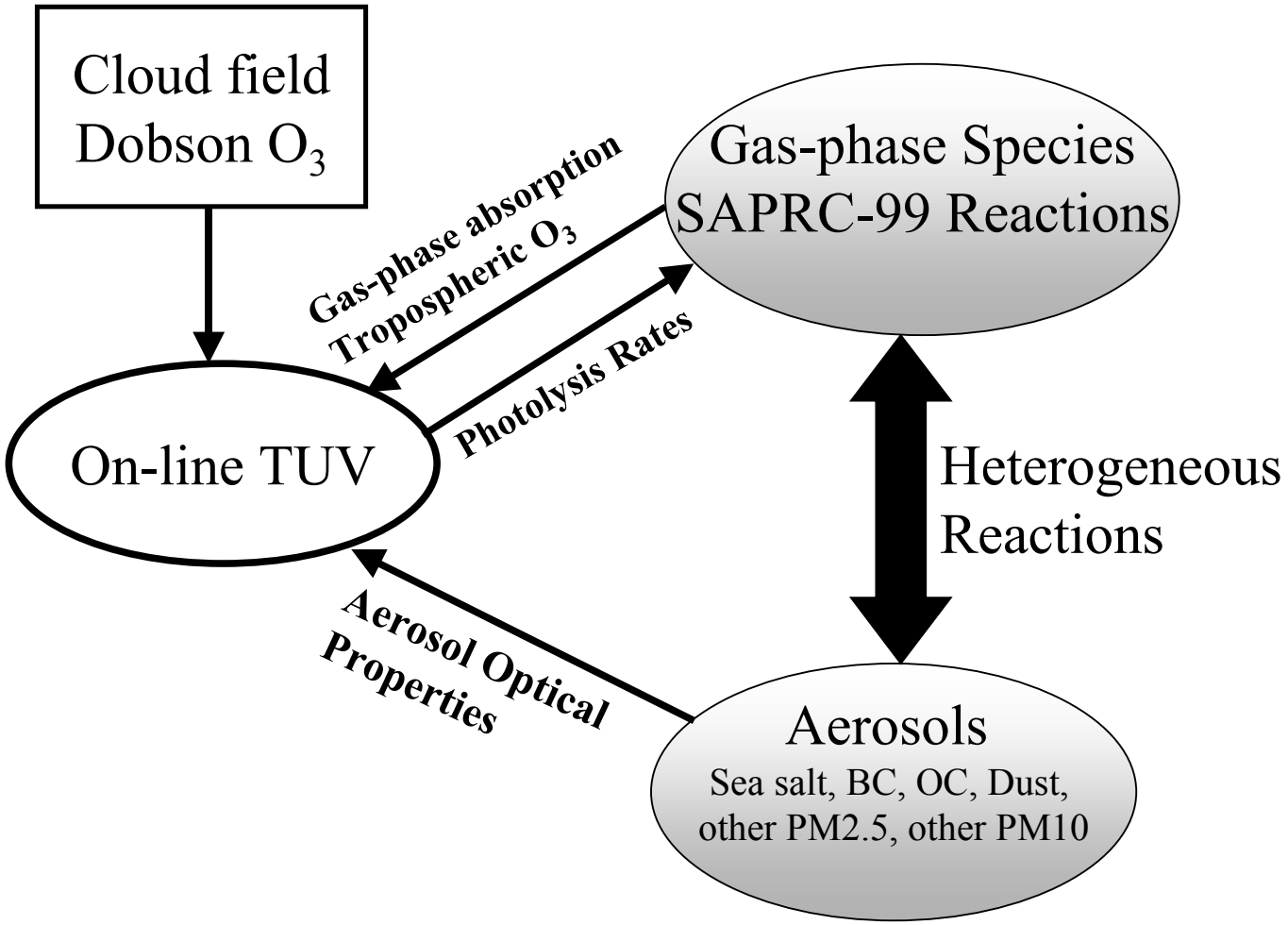
Cloud field
Dobson O_3
Gas-phase Species
SAPRC-99 Reactions
Gas-phase absorption
Tropospheric O_3
Photolysis Rates
On-line TUV
Heterogeneous
Reactions
Aerosol Optical
Properties
Aerosols
Sea salt, BC, OC, Dust,
other PM2.5, other PM10

Figure 1.

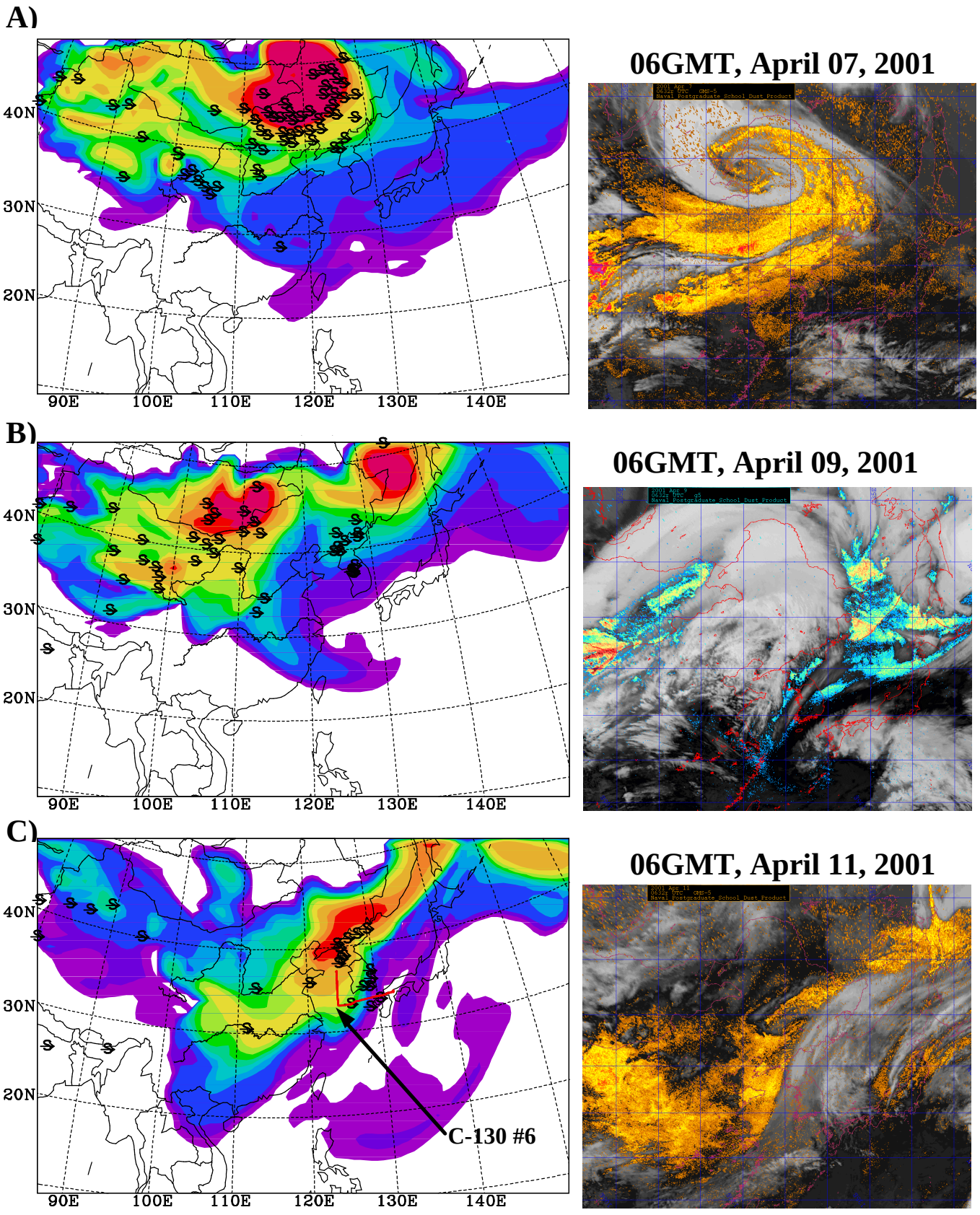
A)
06GMT, April 07, 2001
B)
06GMT, April 09, 2001
C)
06GMT, April 11, 2001
40N
30N
20N
90E
100E
110E
120E
130E
140E
C-130 #6
1.9
4.9
9.7
29
48
79
130
210
340
540
1400
2200
3500
Simulated Dust Concentration (ug/m3) Averaged in the layers below 3km

Figure 2.

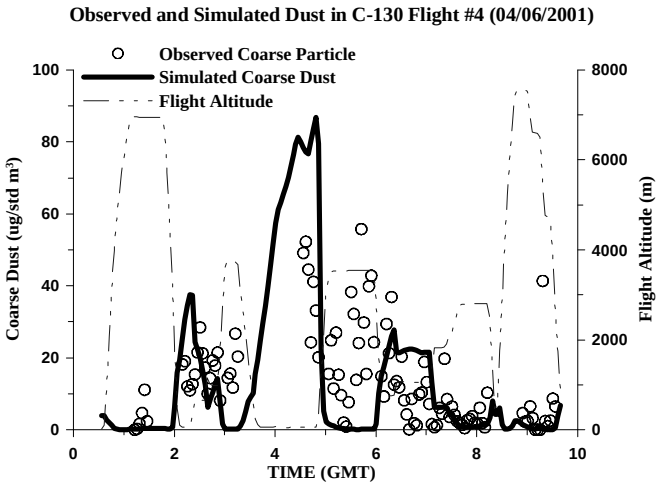
Observed and Simulated Dust in C-130 Flight #4 (04/06/2001)
Observed Coarse Particle
Simulated Coarse Dust
Flight Altitude
Coarse Dust (ug/std m³)
Flight Altitude (m)
TIME (GMT)

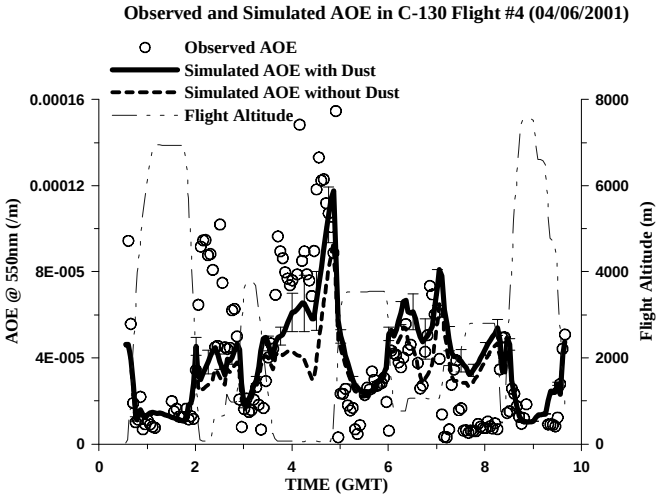
Observed and Simulated AOE in C-130 Flight #4 (04/06/2001)
Observed AOE
Simulated AOE with Dust
Simulated AOE without Dust
Flight Altitude
AOE @ 550nm (/m)
Flight Altitude (m)
TIME (GMT)

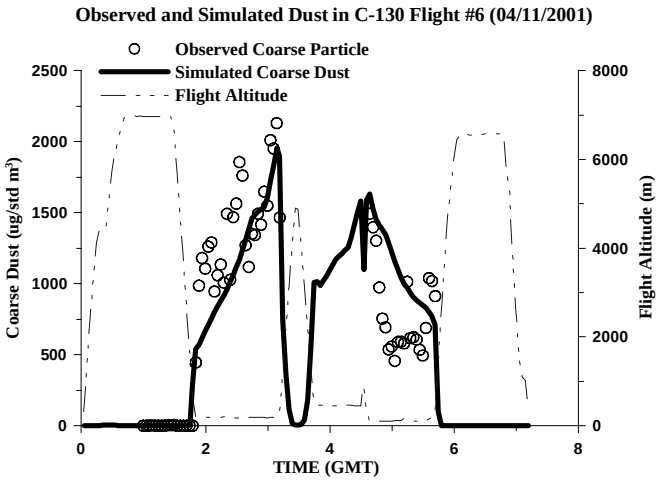
Observed and Simulated Dust in C-130 Flight #6 (04/11/2001)
Observed Coarse Particle
Simulated Coarse Dust
Flight Altitude
Coarse Dust (ug/std m³)
Flight Altitude (m)
TIME (GMT)

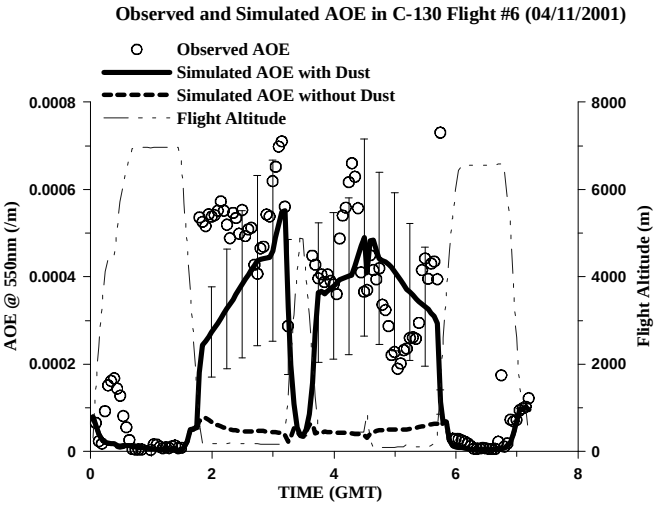
Observed and Simulated AOE in C-130 Flight #6 (04/11/2001)
Observed AOE
Simulated AOE with Dust
Simulated AOE without Dust
Flight Altitude
AOE @ 550nm (/m)
Flight Altitude (m)
TIME (GMT)

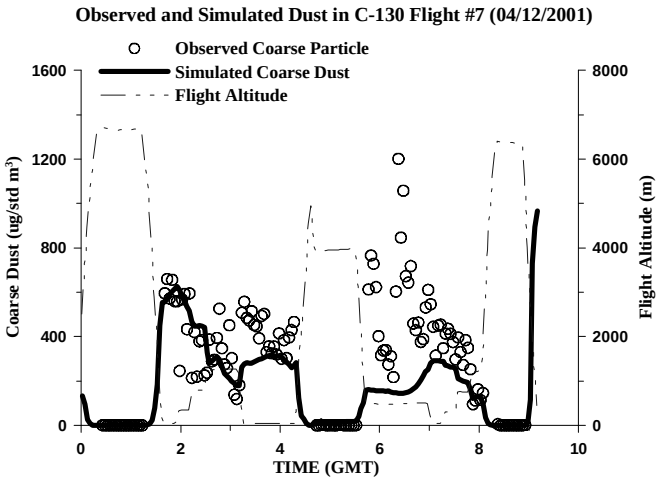
Observed and Simulated Dust in C-130 Flight #7 (04/12/2001)
Observed Coarse Particle
Simulated Coarse Dust
Flight Altitude
Coarse Dust (ug/std m³)
Flight Altitude (m)
TIME (GMT)

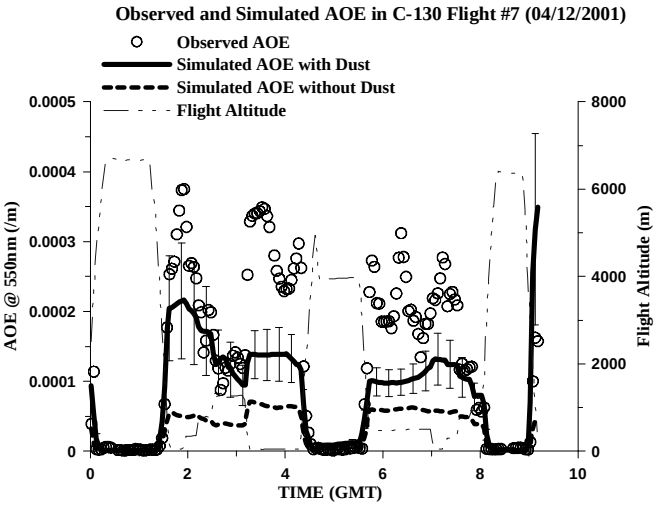
Observed and Simulated AOE in C-130 Flight #7 (04/12/2001)
Observed AOE
Simulated AOE with Dust
Simulated AOE without Dust
Flight Altitude
AOE @ 550nm (/m)
Flight Altitude (m)
TIME (GMT)

Figure 3.

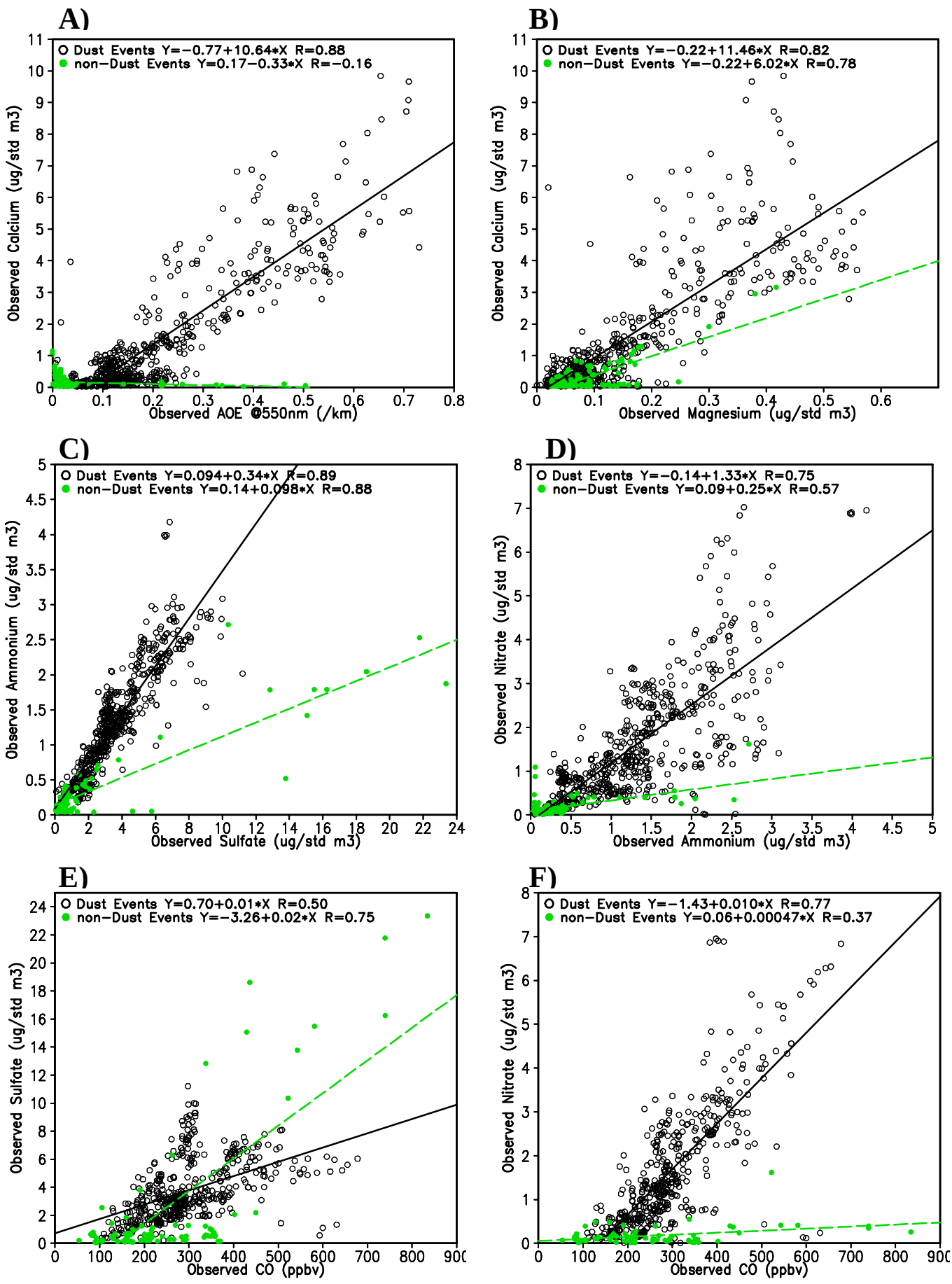
A)
O Dust Events Y=−0.77+10.64*X R=0.88
non−Dust Events Y=0.17−0.33*X R=−0.16
Observed Calcium (ug/std m3)
Observed AOE @550nm (/km)
B)
O Dust Events Y=−0.22+11.46*X R=0.82
non−Dust Events Y=−0.22+6.02*X R=0.78
Observed Calcium (ug/std m3)
Observed Magnesium (ug/std m3)
C)
O Dust Events Y=0.094+0.34*X R=0.89
non−Dust Events Y=0.14+0.098*X R=0.88
Observed Ammonium (ug/std m3)
Observed Sulfate (ug/std m3)
D)
O Dust Events Y=−0.14+1.33*X R=0.75
non−Dust Events Y=0.09+0.25*X R=0.57
Observed Nitrate (ug/std m3)
Observed Ammonium (ug/std m3)
E)
O Dust Events Y=0.70+0.01*X R=0.50
non−Dust Events Y=−3.26+0.02*X R=0.75
Observed Sulfate (ug/std m3)
Observed CO (ppbv)
F)
O Dust Events Y=−1.43+0.010*X R=0.77
non−Dust Events Y=0.06+0.00047*X R=0.37
Observed Nitrate (ug/std m3)
Observed CO (ppbv)

Figure 4.

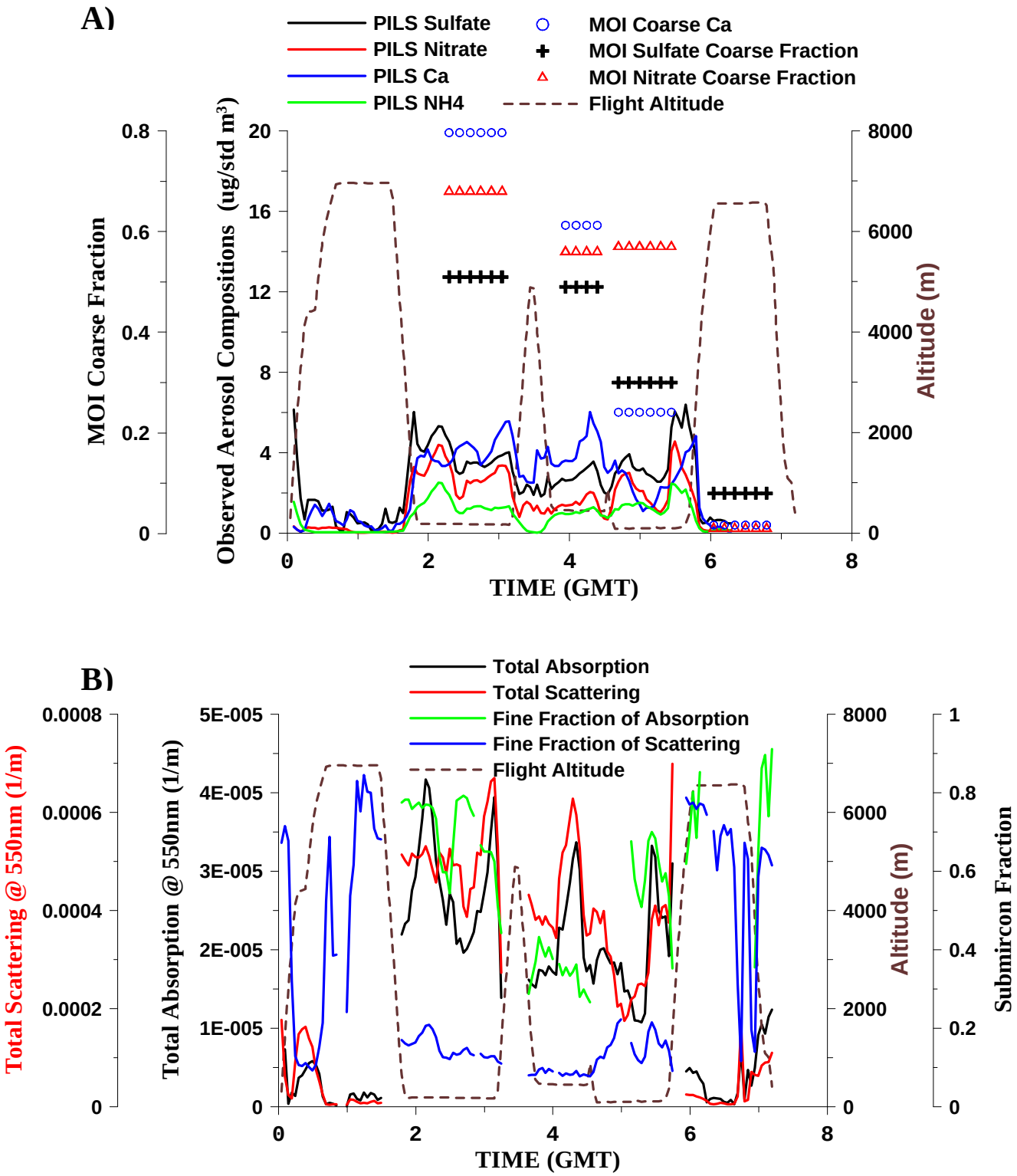
A)
PILS Sulfate
PILS Nitrate
PILS Ca
PILS NH4
MOI Coarse Ca
MOI Sulfate Coarse Fraction
MOI Nitrate Coarse Fraction
Flight Altitude
MOI Coarse Fraction
Observed Aerosol Compositions (ug/std m3)
Altitude (m)
TIME (GMT)
B)
Total Absorption
Total Scattering
Fine Fraction of Absorption
Fine Fraction of Scattering
Flight Altitude
Total Scattering @ 550nm (1/m)
Total Absorption @ 550nm (1/m)
Altitude (m)
Submircon Fraction
TIME (GMT)

Figure 5.

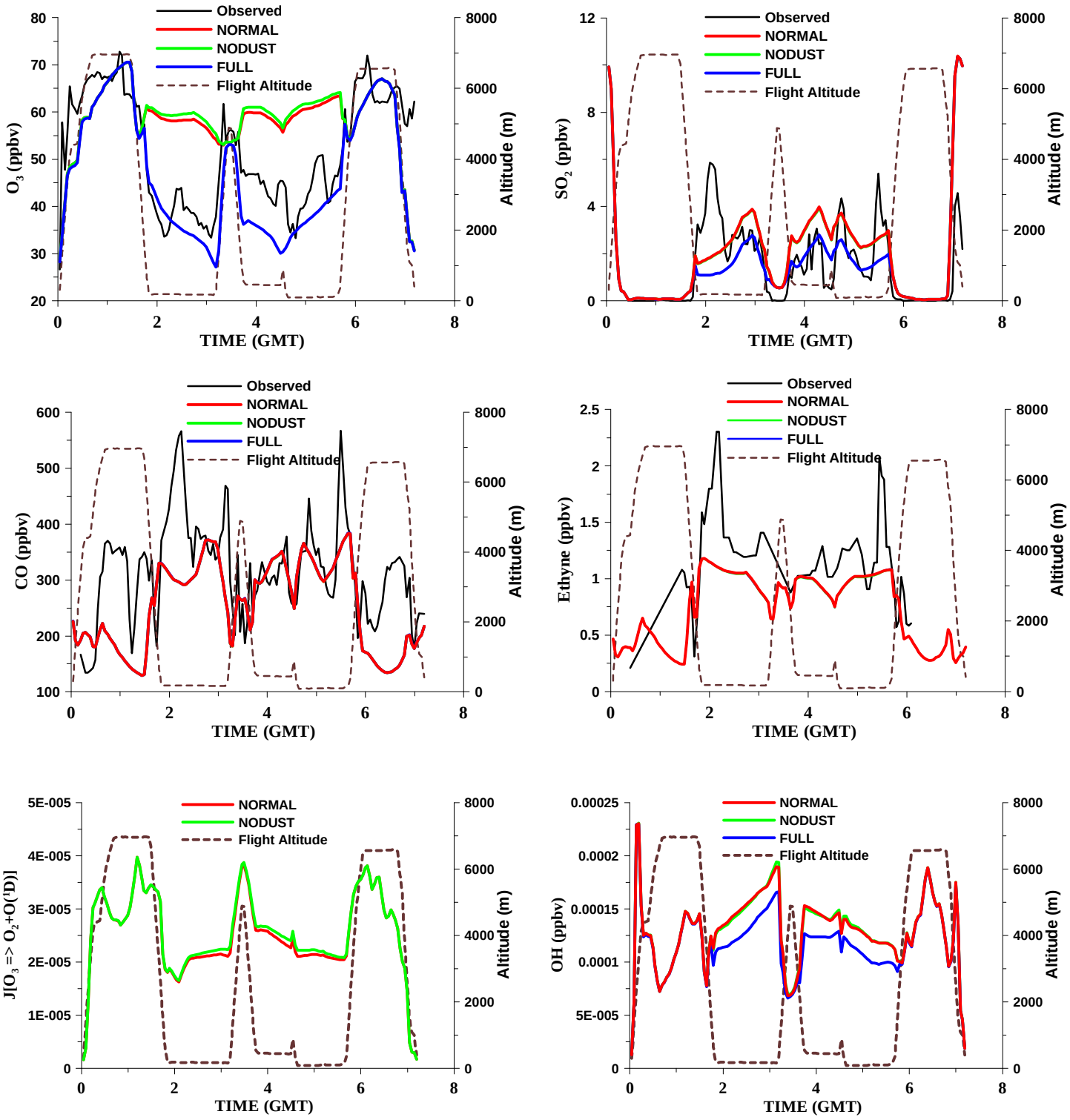
Observed
NORMAL
NODUST
FULL
Flight Altitude
O3 (ppbv)
SO2 (ppbv)
CO (ppbv)
Ethyne (ppbv)
OH (ppbv)
J[O3 => O2+O(1D)]
Altitude (m)
TIME (GMT)

Figure 6.

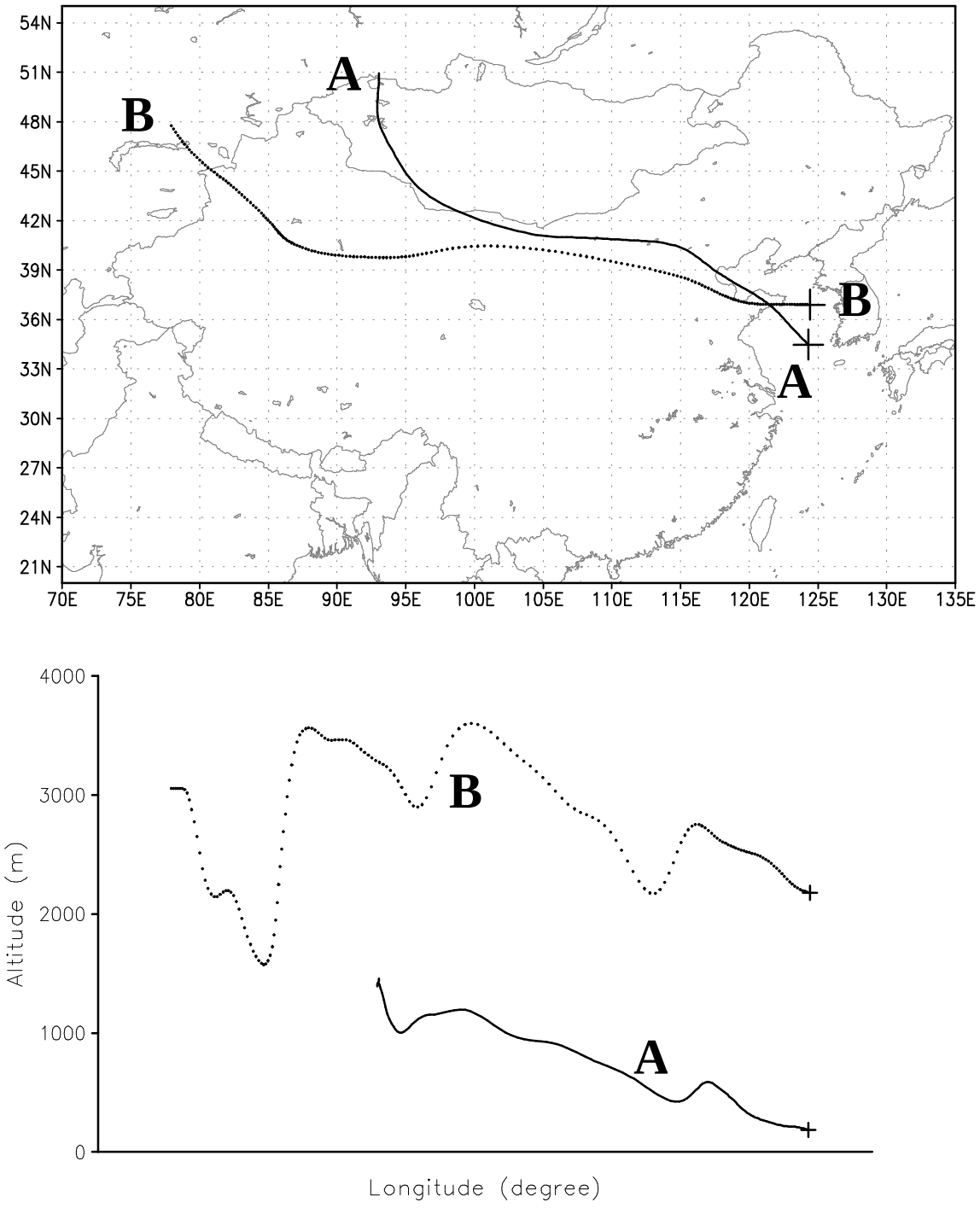
54N
51N
48N
45N
42N
39N
36N
33N
30N
27N
24N
21N
70E
75E
80E
85E
90E
95E
100E
105E
110E
115E
120E
125E
130E
135E
A
B
B
A
4000
3000
2000
1000
0
Altitude (m)
B
A
Longitude (degree)

Figure 7.

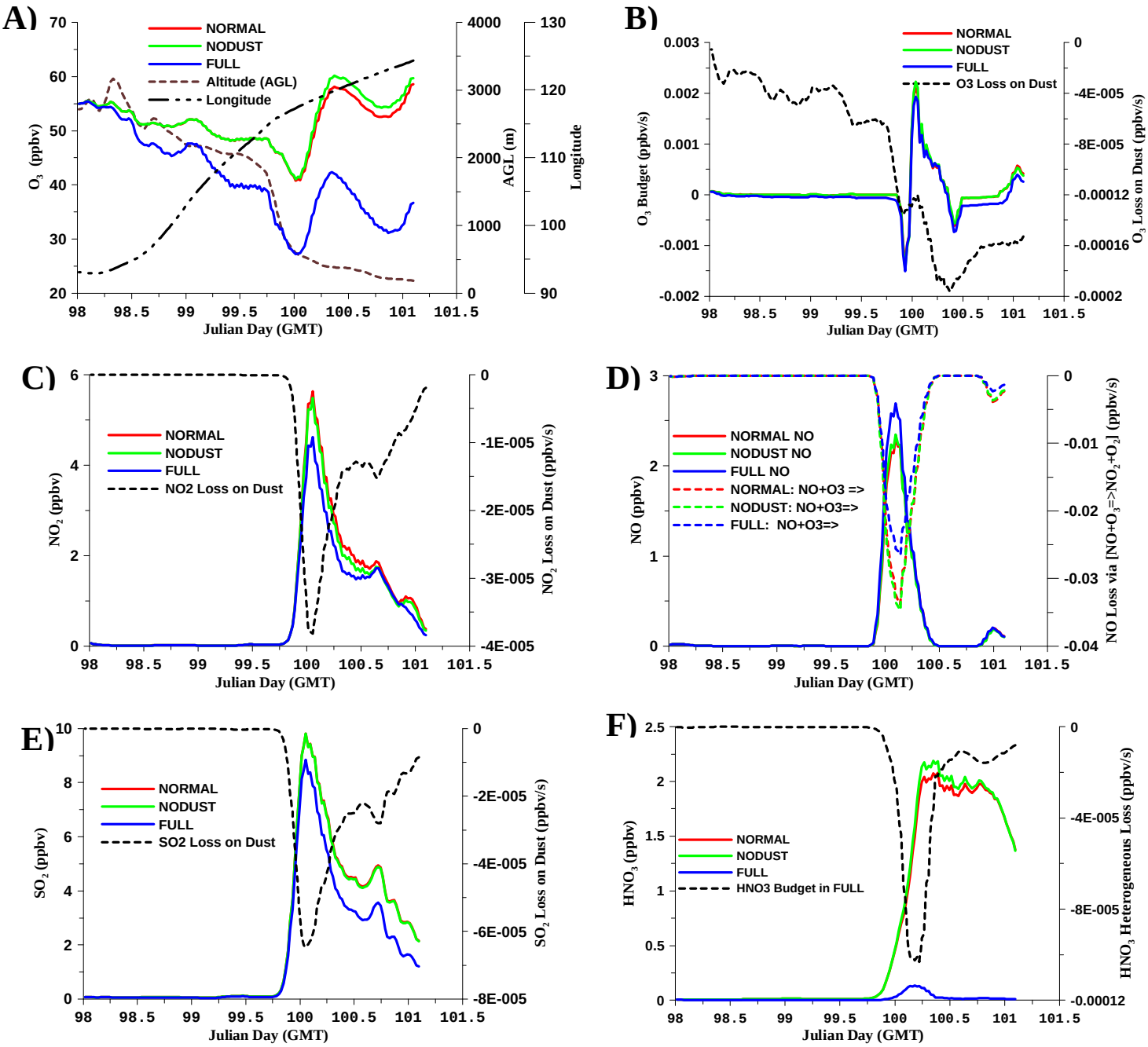

Figure 8 (continued on next Page)

Figure 8 (continued)

G)

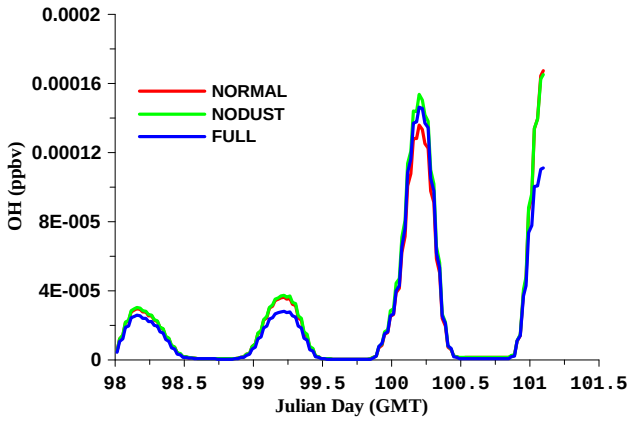

H)

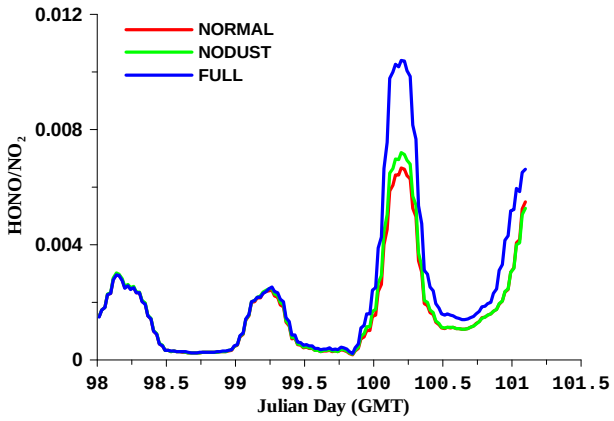

I)

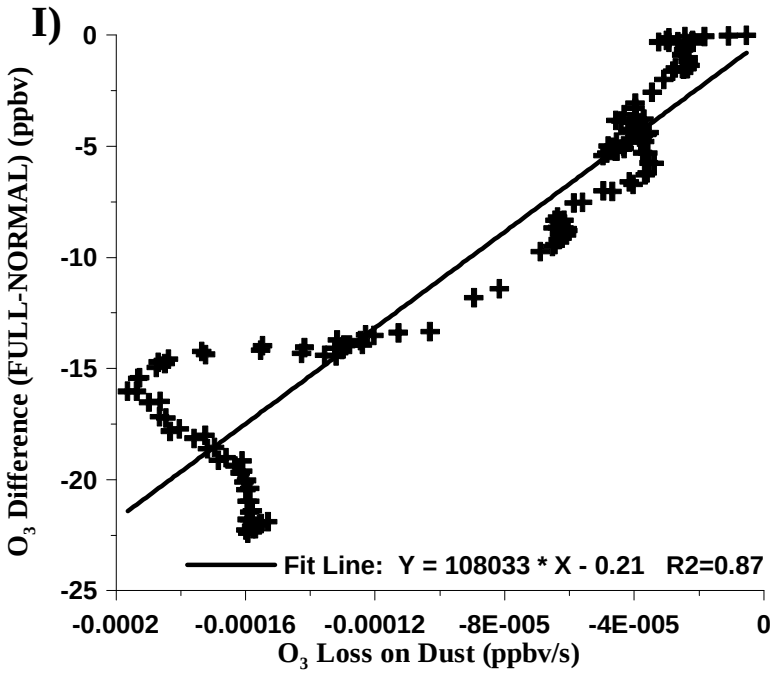

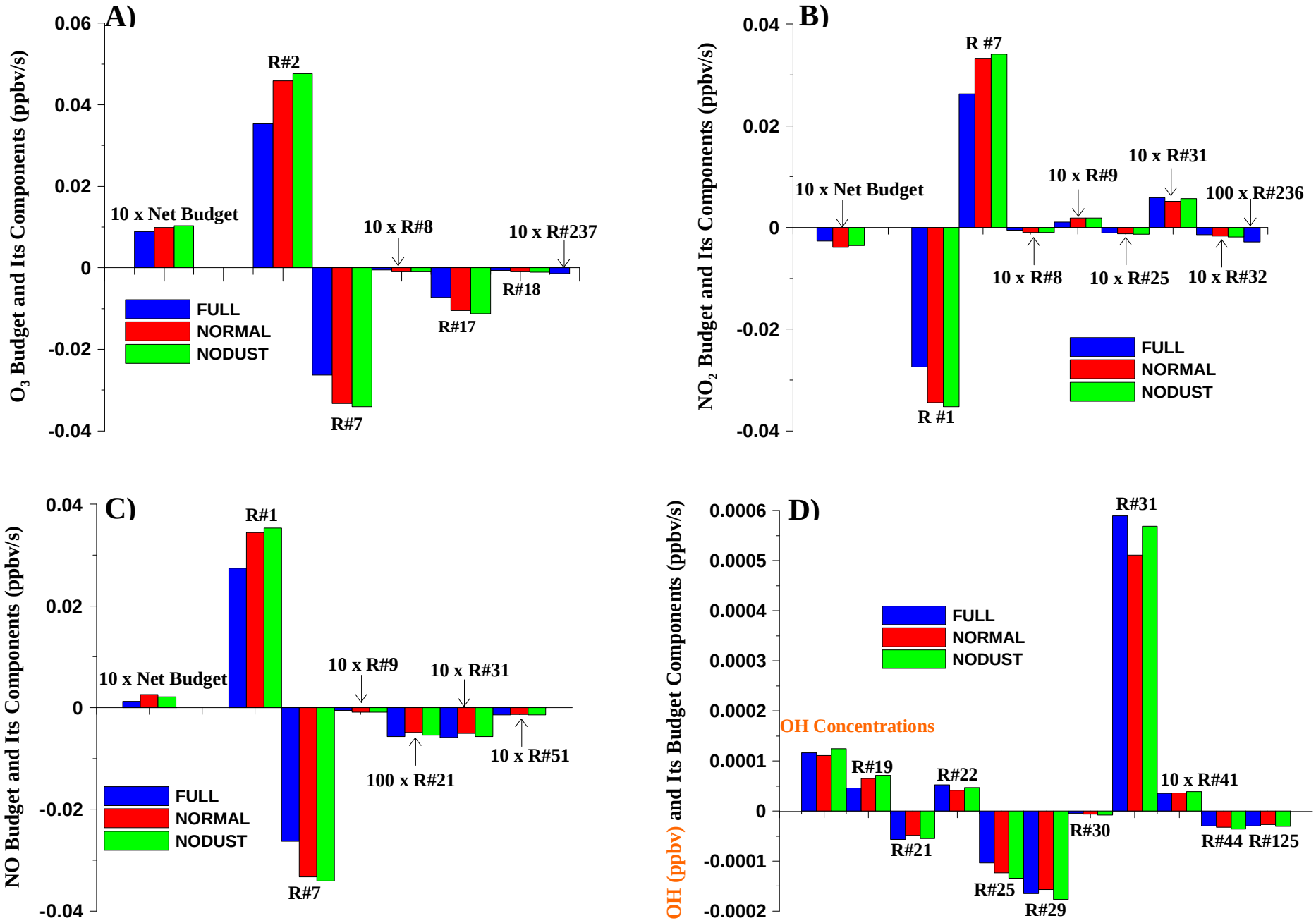
A)
O3 Budget and Its Components (ppbv/s)
0.06
0.04
0.02
0
-0.02
-0.04
10 x Net Budget
R#2
10 x R#8
10 x R#237
R#18
R#17
R#7
FULL
NORMAL
NODUST
B)
NO2 Budget and Its Components (ppbv/s)
0.04
0.02
0
-0.02
-0.04
R #7
10 x R#31
10 x R#9
10 x Net Budget
100 x R#236
10 x R#8
10 x R#25
10 x R#32
R #1
FULL
NORMAL
NODUST
C)
NO Budget and Its Components (ppbv/s)
0.04
0.02
0
-0.02
-0.04
R#1
10 x R#9
10 x R#31
10 x Net Budget
100 x R#21
10 x R#51
R#7
FULL
NORMAL
NODUST
D)
OH (ppbv) and Its Budget Components (ppbv/s)
0.0006
0.0005
0.0004
0.0003
0.0002
0.0001
0
-0.0001
-0.0002
R#31
FULL
NORMAL
NODUST
OH Concentrations
R#19
R#22
10 x R#41
R#21
R#30
R#44 R#125
R#25
R#29

Figure 9.

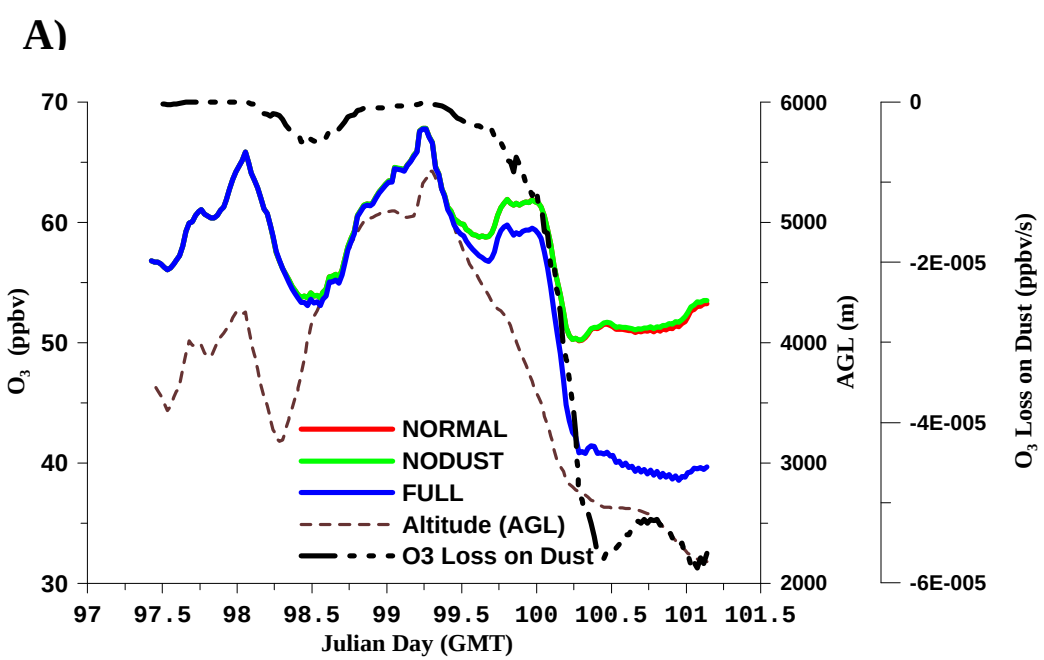
A)
70
60
50
40
30
O_3 (ppbv)
97
97.5
98
98.5
99
99.5
100
100.5
101
101.5
Julian Day (GMT)
6000
5000
4000
3000
2000
AGL (m)
0
-2E-005
-4E-005
-6E-005
O_3 Loss on Dust (ppbv/s)
NORMAL
NODUST
FULL
Altitude (AGL)
O3 Loss on Dust

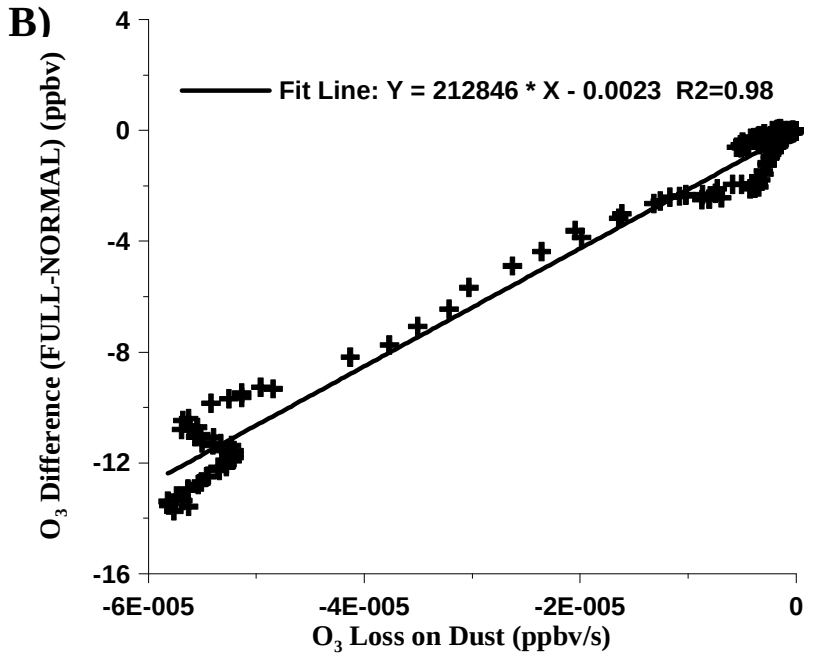
B)
4
0
-4
-8
-12
-16
O_3 Difference (FULL-NORMAL) (ppbv)
Fit Line: Y = 212846 * X - 0.0023 R2=0.98
-6E-005
-4E-005
-2E-005
0
O_3 Loss on Dust (ppbv/s)

Figure 10.

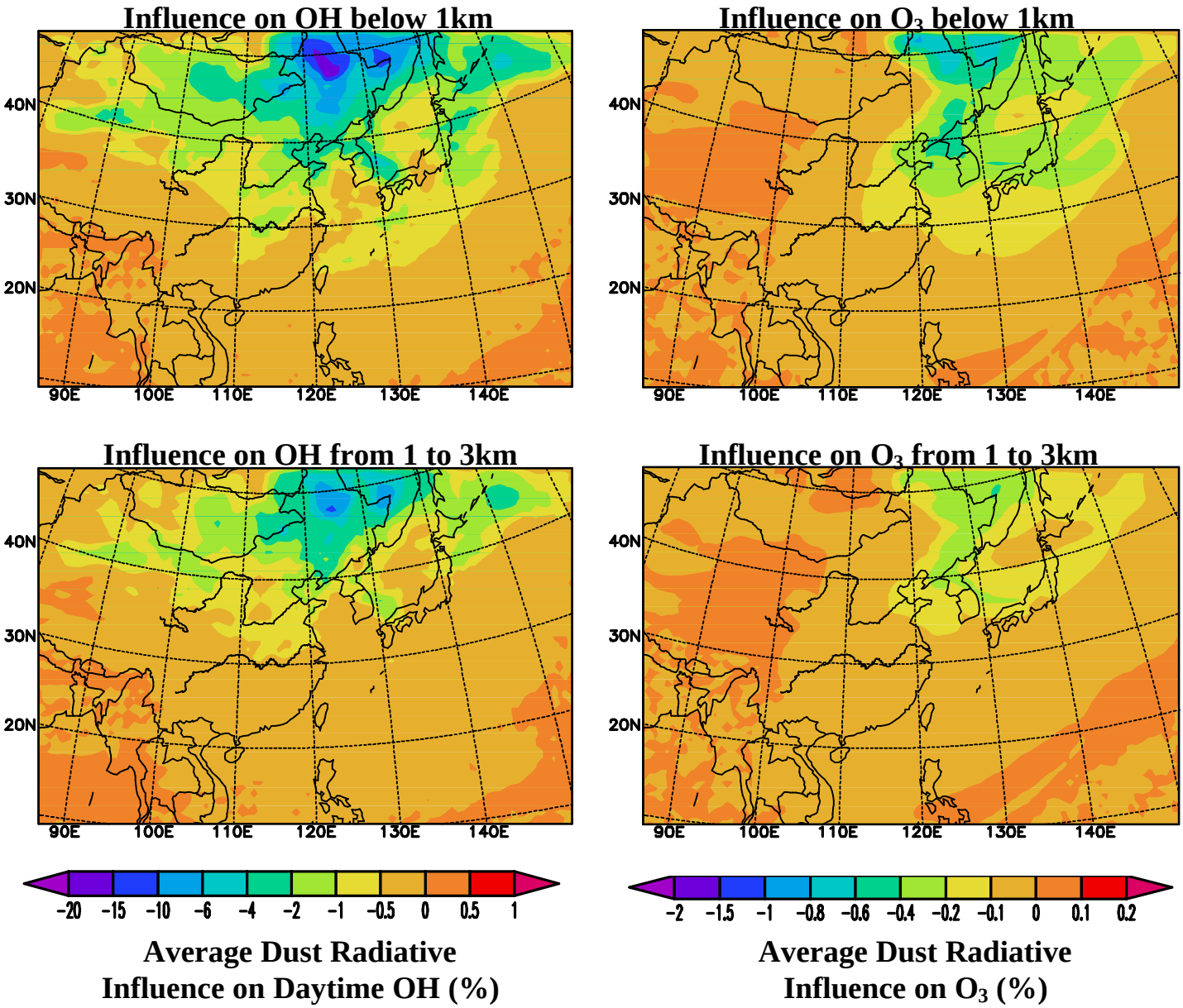
Influence on OH below 1km
Influence on O3 below 1km
Influence on OH from 1 to 3km
Influence on O3 from 1 to 3km
40N
30N
20N
90E
100E
110E
120E
130E
140E
-20 -15 -10 -6 -4 -2 -1 -0.5 0 0.5 1
Average Dust Radiative Influence on Daytime OH (%)
-2 -1.5 -1 -0.8 -0.6 -0.4 -0.2 -0.1 0 0.1 0.2
Average Dust Radiative Influence on O3 (%)

Figure 11.

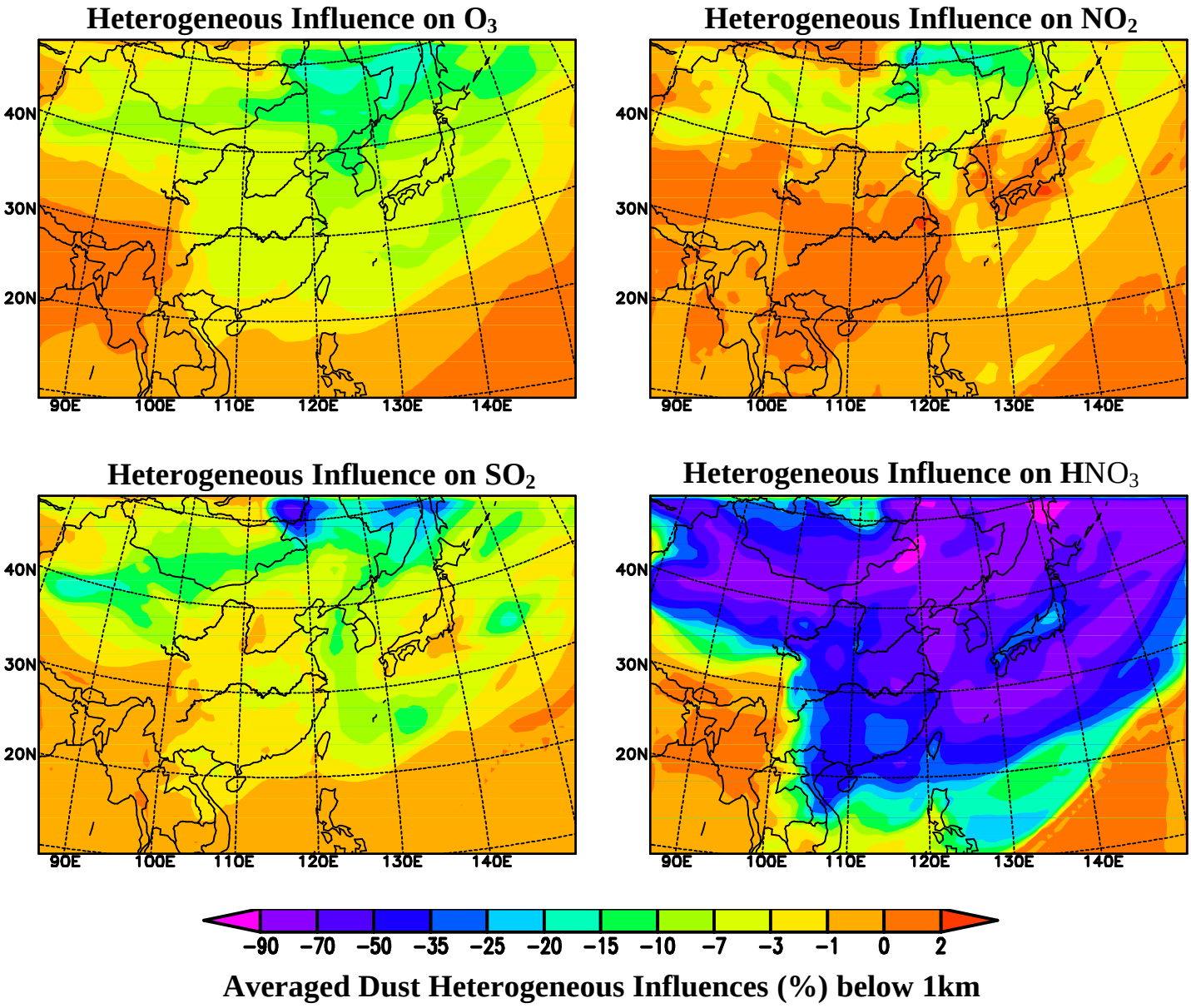
Heterogeneous Influence on O_3
Heterogeneous Influence on NO_2
Heterogeneous Influence on SO_2
Heterogeneous Influence on HNO_3
40N
30N
20N
90E
100E
110E
120E
130E
140E
−90 −70 −50 −35 −25 −20 −15 −10 −7 −3 −1 0 2
Averaged Dust Heterogeneous Influences (%) below 1km

Figure 12.

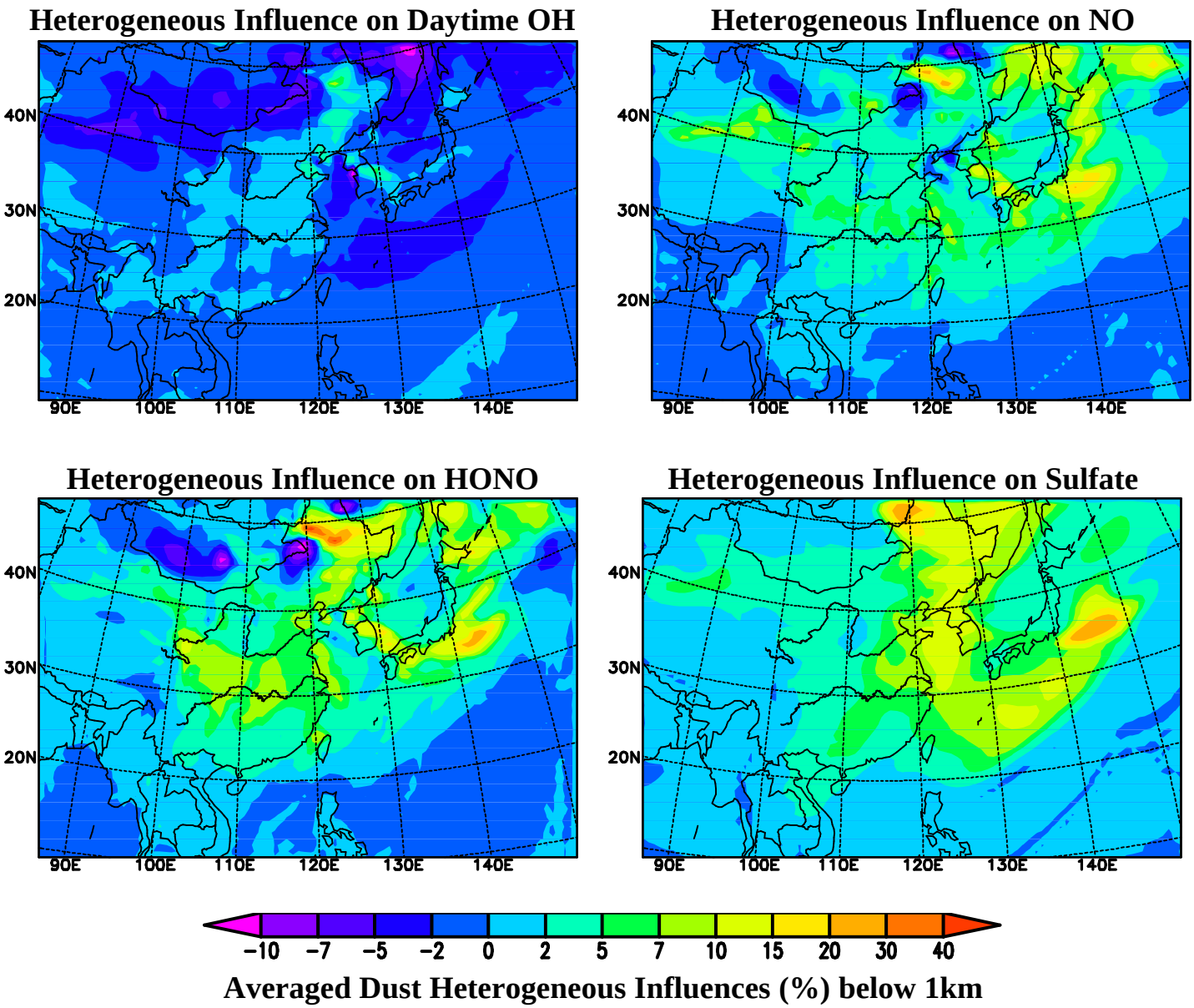
Heterogeneous Influence on Daytime OH
Heterogeneous Influence on NO
Heterogeneous Influence on HONO
Heterogeneous Influence on Sulfate
40N
30N
20N
90E
100E
110E
120E
130E
140E
−10 −7 −5 −2 0 2 5 7 10 15 20 30 40
Averaged Dust Heterogeneous Influences (%) below 1km

Figure 13.